Tectonophysics 929 (2026) 231175

Contents lists available at ScienceDirect

Tectonophysics

journal homepage: www.elsevier.com/locate/tecto

GST-1: A high-resolution global sediment thickness model

Dale E. Bird [a,b,c,*], Walter D. Mooney [c]

[a] Department of Earth and Atmospheric Sciences, University of Houston, USA
[b] Bird Geophysical, Houston, TX 77204, USA
[c] USGS, Earthquake Science Center, Moffett Field, California 94035, USA

ARTICLE INFO

Keywords:
Global model
Sediment thickness
Gravity model
3D Inversion

ABSTRACT

Global Sediment Thickness 1 (GST-1) is a high-resolution sedimentary thickness model calculated on a 0.125° x 0.125° grid. It modifies the sediment thickness of the 1° x 1° Earth Crustal Model 1 (ECM1) by means of 3D inversions of free air gravity anomalies. GST-1 is calculated by performing structural inversions on high-density contrasts across two crustal boundaries: the sediment – basement interface and the crystalline crust – upper mantle interface. The inversions are calculated in each of ten overlapping 3D models that span the globe. These ten models are merged to obtain the GST-1 global model, providing an eight-fold increase in lateral spatial resolution in comparison with ECM1 and CRUST 1.0. Our sediment thickness model exploits the nearly continuous sampling of gravity data when compared to the irregular, sparse sampling of seismic refraction data. Sediment thickness values in GST-1 are in excellent agreement with independently derived cross sections from well-studied sedimentary basins, and within expected resolution limits of seismic refraction data. GST-1 offers a robust, high resolution global model of sedimentary thickness to support studies of sedimentary basins.

1. Introduction

Sedimentary basins cover substantial portions of the Earth's surface and preserve evidence for the geologic, tectonic, biological, and climate history of the planet (Busby and Azor, 2012; Cloetingh and Negendank, 2010; Foote and Miller, 2006; Grozinger and Jordan, 2020; Hyman, 2017). Diverse natural resources are derived from sedimentary basins, such as hydrocarbons, minerals, geothermal energy, water, and arable soil (Marshak, 2022; Miall, 2000, 2010). The abundance and distribution of these natural resources are influenced by factors that include the basin's depositional and structural history (Bally et al., 2020; Busby and Azor, 2012). Basin analyses are used to decode this record via the study of sedimentary host strata to document subsidence history, stratigraphic architecture, and paleogeographic evolution (Miall, 2000, 2010). Given the importance of sedimentary basins, a high-resolution global sedimentary thickness model is a valuable contribution to support analyses of basin formation and resource potential.

An early version of a global crust model is CRUST 5.1 (Mooney et al., 1998), which is provided on 5° x 5° grids with eight layers: ice, water, low velocity sediment, high velocity sediment, upper crystalline crust, middle crystalline crust, lower crystalline crust, and upper mantle. Rock properties in each layer are P-wave velocities, S-wave velocities, and density. Spatial sampling of this model was decreased to 2 degrees by Bassin et al. (2000), and then to 1 degree by Laske et al. (2012). Recently, after integrating additional seismic velocity measurements (19,200 total), Earth Crust Model 1 (ECM1) has been introduced (Mooney et al., 2023), however spatial sampling remains at 1 degree. In marine only regions, a global sediment thickness model (GlobSEd) was introduced on a 5 min grid (Straume et al., 2019). ECM1 adopts GlobSed as the primary source of sediment thickness values in marine areas, and the sedimentary thickness models of Laske et al. (2012) and Molinari and Morelli (2011) for terrestrial areas. Many global crust and lithosphere models incorporate elements of CRUST 1.0 and CRUST 2.0 (Afonso et al., 2019; Fullea et al., 2021; Kaban et al., 1999; Pasyamos et al., 2014; Reguzzoni and Sampietro, 2015).

Here we present the Global Sediment Thickness 1 (GST-1) model, an updated representation of the sedimentary layer of ECM1 (Mooney et al., 2023), provided on 0.125° x 0.125° grid cells. We use continuous gravity data (Fig. 1) to modify the basement horizon at the base of the sediment layer, via 3D gravity inversions. In this way, we calculate a global sediment thickness with greater detail on basin geometries than available models.

For computational accuracy, we calculate ten overlapping regional 3D models that span the globe (Fig. 2). The 3D models consist of five

* Corresponding author at: Department of Earth and Atmospheric Sciences, University of Houston, USA.
E-mail address: dale@birdgeo.com (D.E. Bird).

https://doi.org/10.1016/j.tecto.2026.231175
Received 23 July 2025; Received in revised form 17 March 2026; Accepted 19 March 2026
Available online 27 March 2026

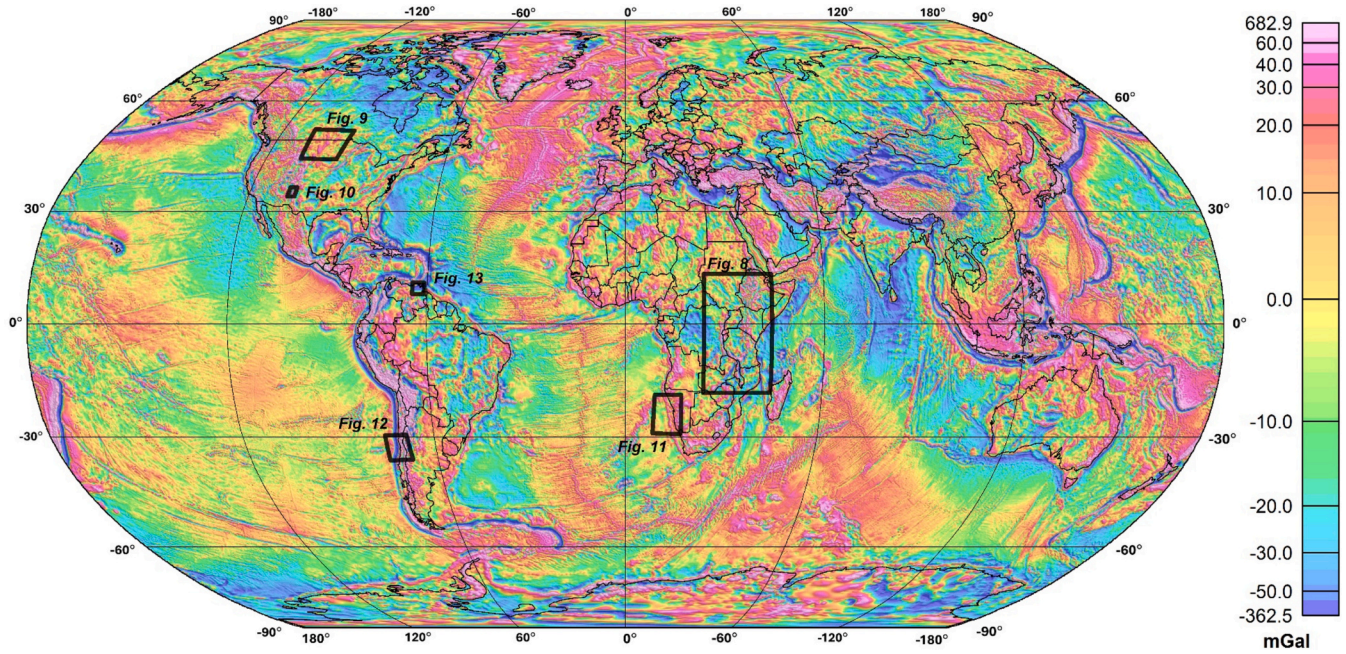

Fig. 1. Merged free air gravity anomalies (Kenyon et al., 2008; Pavlis et al., 2012; Scheinert et al., 2016). The lateral continuity of these gravity data makes possible the refinement of the sediment thickness estimates based on unevenly distributed seismic control. Figs. 8–13 locations are outlined by heavy black polygons.

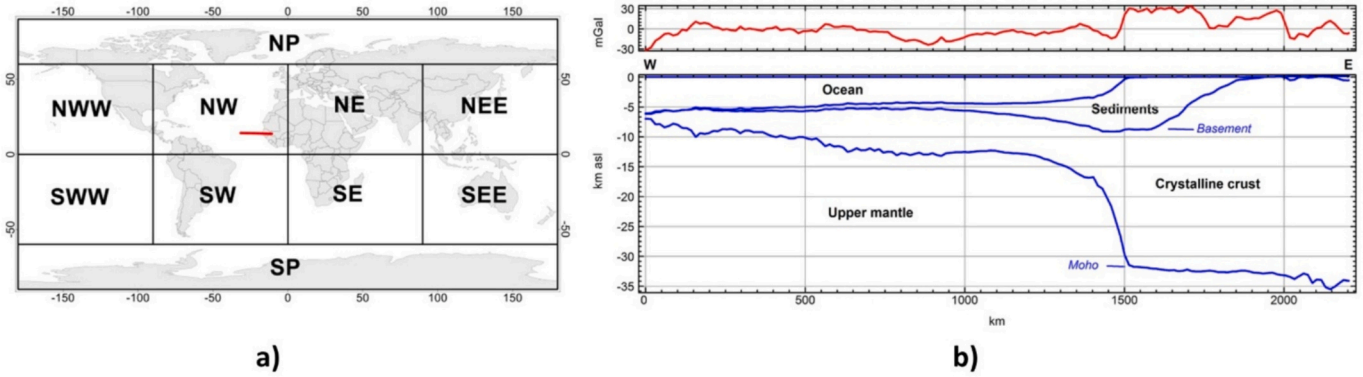

Fig. 2. Locations of regional inversion models: a) ten 3D model areas (map boundaries: latitude, 0° and ± 60°; longitude, 0°, ±90°, and ± 180°), and cross section location (red line); b) cross section and free air gravity profile (red) through west Africa, regional 3D model NW (also mapped in Fig. 6), each of the ten regional 3D models are composed of five or six layers, separated by four or five horizons (blue): surface, top of ice (polar models only), topography, basement, and base of crust. (For interpretation of the references to colour in this figure legend, the reader is referred to the web version of this article.)

horizons: ice (polar regions only), topography and sea surface, bathymetry, top of crystalline crust (basement), and base of crust. Single layer densities are applied except for sediment and upper mantle layers, which vary as functions of thickness and lithospheric age, respectively. Two sets of 3D structural inversions of gravity data are performed on the models: 1) base of crust inversion, guided primarily by the long wavelength gravity anomalies, and 2) basement inversion, which is guided primarily by shorter wavelength anomalies. We compare our results with cross sections through well studied basins, and with established global models.

2. Gravity data

Most of the Earth is covered by the EGM2008 free air gravity grid (Pavlis et al., 2012). The EGM2008 data compilation includes gravity values over land by incorporating GRACE satellite gravity data and digital elevation models, and over marine areas using gravity data derived from satellite altimetry (Anderson et al., 2010; Forsberg, 1984; Lemoine et al., 1998; Mayer-Gürr, 2007; Rapp, 1997; Sandwell and Smith, 2009). However, EGM2008 polar data is inadequate for this study due to limited satellite coverage, therefore, EGM2008 data are merged with Arctic and Antarctic free air anomalies (Fig. 1) (Kenyon et al., 2008; Scheinert et al., 2016). Data compiled in the Arctic Gravity Project from land, marine, and airborne sources are updated by Kenyon et al. (2008). Similarly, gravity data are compiled over Antarctica to include land, marine, airborne, and satellite surveys (Scheinert et al., 2016). Reported gravity data resolutions range from ±3.6 mGal over the southern polar region (Scheinert et al., 2016), to ±6 mGal over the northern polar region (Forsberg and Skourup, 2005), to ±34 mGal for EGM2008 (Pavlis et al., 2012). The broad range for EGM2008 is primarily due to the lack of data over mountainous regions (Pavlis et al., 2012). This deficiency was addressed by Liang et al. (2020) by integrating GOCE and GRACE satellite data over terrestrial areas, as well as updated gravity derived from satellite altimetry (Sandwell et al., 2014), in the SGG-UGM-2 gravity model. We found that differences between EGM3008 and SGG-UGM-2 over three large regions of North America,

Table 1
Global crust model layer densities, and density contrasts. Density range, mean and standard deviation (std) are listed for sediment, crystalline crust, and upper mantle layers, as well as horizontal density gradient, $\sqrt{(\rho^x \cdot \rho^x + \rho^y \cdot \rho^y)}$, for each layer. Mean and standard deviation of density contrasts at basement and base crust surface (crust-mantle boundary) are listed, as well as horizontal density gradients along these boundaries. Units in Table 1 are g/cm^3 per degree, which means 1 g/cm^3 per degree ≈ 0.009 g/cm^3 per km. Models include GST-1 (this study), ECM1 (Mooney et al., 2023), WINTERC-G (Fullea et al., 2021), LithoRef18 (Afonso et al., 2019), CRUST 1.0 (Laske et al., 2012), CRUST 2.0 (Bassin et al., 2000), and CRUST 5.1 (Mooney et al., 1998). GST-1 uses a single density for its crystalline crust layer. LithoRef18 and WINTERC-G models do not include a separate sediment layer.

	GST-1	ECM1	WINTERC-G	LithoRef18	CRUST 1.0	CRUST 2.0	CRUST 5.1
Sediment layer, range	2.150–2.600	1.740–2.562	n/a	n/a	1.596–2.484	1.949–2.419	1.963–2.555
Sediment layer, mean ± std	2.222 ± 0.088	2.078 ± 0.142	n/a	n/a	2.020 ± 0.184	2.173 ± 0.130	2.176 ± 0.132
Sediment layer gradient, mean ± std	0.029 ± 0.039	0.047 ± 0.045	n/a	n/a	0.046 ± 0.053	0.014 ± 0.017	0.010 ± 0.009
Crust layer, range	2.825	2.734–2.870	2.650–3.050	2.580–3.056	2.690–2.953	2.805–3.004	2.807–3.026
Crust layer, mean ± std	n/a	2.793 ± 0.036	2.861 ± 0.068	2.844 ± 0.076	2.820 ± 0.030	2.870 ± 0.028	2.870 ± 0.029
Crust layer gradient, mean ± std	n/a	0.006 ± 0.009	0.043 ± 0.042	0.019 ± 0.014	0.012 ± 0.017	0.005 ± 0.006	0.003 ± 0.004
Mantle, range	3.000–3.300	3.181–3.384	3.213–3.400	3.210–3.387	3.015–3.461	3.237–3.460	3.220–3.437
Mantle, mean	3.296 ± 0.014	3.305 ± 0.018	3.339 ± 0.021	3.325 ± 0.029	3.332 ± 0.047	3.365 ± 0.029	3.364 ± 0.028
Mantle gradient, mean ± std	0.006 ± 0.040	0.006 ± 0.011	0.014 ± 0.026	0.006 ± 0.006	0.013 ± 0.019	0.006 ± 0.008	0.004 ± 0.004
Basement contrast, mean	0.603 ± 0.088	0.715 ± 0.124	n/a	n/a	0.799 ± 0.183	0.696 ± 0.118	0.695 ± 0.118
Basement contrast gradient, mean ± std	0.029 ± 0.039	0.047 ± 0.045	n/a	n/a	0.050 ± 0.054	0.016 ± 0.017	0.010 ± 0.009
Base crust contrast, mean ± std	0.471 ± 0.014	0.511 ± 0.028	0.478 ± 0.074	0.481 ± 0.078	0.512 ± 0.052	0.496 ± 0.028	0.493 ± 0.032
Base crust contrast gradient, mean ± std	0.006 ± 0.040	0.009 ± 0.013	0.047 ± 0.049	0.019 ± 0.014	0.018 ± 0.021	0.005 ± 0.008	0.004 ± 0.004

Africa and Asia are small, ranging between 0.73% and 1.33%. We provide a thorough analysis in Supplementary Information, Section SI-1.

3. Methods

Recognizing that a significant density contrast exists at the base of most sedimentary basins (i.e., at the top of the crystalline crust, also referred to as the basement surface), we seek to isolate gravity anomalies produced by this surface. We perform 3D gravity inversions of these isolated anomalies to modify the depth of the basement surface, thus reshaping the sedimentary layer thickness between the topography and basement. Regarding these inversions, the inherent ambiguity in gravity models can be reduced by implementing *a priori* conditions to gravity inversions (Barbosa and Silva, 1994; Li and Oldenburg, 1998; Pedersen, 1979). The accuracy of the *a priori* information is important to avoid inversion artifacts (e.g., local minima). Our ten *a priori* regional crustal models (Fig. 2a) include a base of crust that is based on well-established principles of isostasy (Blakely, 1995). While simple isostatic crustal models are generally accurate globally, we acknowledge that inaccuracies may exist in some regions.

Density and P-wave velocity variations in the upper mantle are associated with temperature variations (Fowler, 2005; Perry et al., 2006; Prodehl and Mooney, 2012). A sufficient increase in upper mantle temperature will cause partial melting, thus decreasing density and velocity. Regional high temperature anomalies are correlated with thinned crust and reduced upper mantle density; for example, the Afar Depression and Great Basin of the western USA (Ebinger et al., 2010; Mooney and Kaban, 2010). Conversely, regional low temperatures are correlated with thicker crust and cooler, higher density upper mantle, such as the Canadian Shield and eastern Europe (Mooney and Kaban, 2010; Tesauro et al., 2009). In these examples, heat flow anomalies and correlated crustal thickness variations are well controlled by global data sets described by Mooney et al. (2023) and the Global Heat Flow Data Assessment Group (2024). However, the global coverage of these databases is not uniform, and large gaps exist over the Earth's oceans and remote terrestrial regions. Yet, evolution of oceanic lithosphere over time is well understood (Dick et al., 2010; Heirtzler, 1969; Heirtzler et al., 1968; Moores and Twiss, 1995; Müller et al., 2016; Reid and Jackson, 1981), including variations of upper mantle temperature and crustal subsidence as functions of lithospheric age (McKenzie, 1967; Sclater et al., 1980; Stein and Stein, 1992; Zhou et al., 2020). We therefore incorporate these oceanic temperature and subsidence variations in our models (Stein and Stein, 1992).

Density variations that exist in the sedimentary and crystalline layers of the Earth's crust have been tabulated by several authors (Carmichael, 1989; Christensen and Mooney, 1995; Dobrin and Savit, 1988; Hinze et al., 2013; Sharma, 1976; Telford et al., 1976; Turcotte and Schubert, 2002). Sedimentary rock compositions can vary from low density salt (~1.8 to 2.2 g/cm^3), to clastic rocks such as sandstone, siltstone, mudstone and shale (~2.0 to 2.7 g/cm^3), to carbonate rocks, such as limestone and dolomite, which may have a broad range of densities (~1.6 to 2.9 g/cm^3). Density ranges from ~2.6 to 2.9 g/cm^3 in the upper crystalline oceanic and continental crusts (e.g., basalt, granite and gneiss), and from ~2.8 to 3.0 g/cm^3 in lower crystalline crust (e.g., gabbro, amphibolite, and granulite). Given the complexity associated with these ranges of crystalline crust density, we adopt a single density of 2.825 g/cm^3 for the entire crystalline crust layer in all of our 3D models, which is consistent with an extensive analysis of 48 crystalline rock types at depths ranging from 5 to 50 km, and temperatures ranging from 20° to 925 °C (Christensen and Mooney, 1995).

Table 1 lists density variations within layers (sediment, crystalline crust, and upper mantle) from seven global models: GST-1 (this study), ECM1 (Mooney et al., 2023), WINTERC-G (Fullea et al., 2021), LithoRef18 (Afonso et al., 2019), CRUST 1.0 (Laske et al., 2012), CRUST 2.0 (Bassin et al., 2000), and CRUST 5.1 (Mooney et al., 1998). Key density contrasts are listed as well: the basement surface, and the base of crust (the crust-mantle boundary). Table 1 also includes horizontal gradients, $\sqrt{(\rho^x \cdot \rho^x + \rho^y \cdot \rho^y)}$, within layers and along the basement and base of crust surfaces to illustrate how density varies laterally in the models. Units in Table 1 are g/cm^3 per degree. Converting to g/cm^3 per km: 1 g/cm^3 per degree ≈ 0.009 g/cm^3 per km. Converting the total range of all layer density variations in Table 1 (0.003 to 0.047 g/cm^3 per degree), yields 0.000027 to 0.000423 g/cm^3 per km, which is a vanishingly small density gradient for all model layers. At the basement and base crust horizons however, density contrasts are significant, ranging from 0.603 to 0.799 g/cm^3 and 0.471 to 0.512 g/cm^3, respectively. Horizontal density gradients along basement and base crust surfaces, like layer density gradients, are also small: 0.004 to 0.050 g/cm^3 per degree, or 0.000035 to 0.00045 g/cm^3 per km. We conclude that the gravity inversions will be primarily driven by density contrasts at the basement surface, and secondarily by density contrasts at the base of crust. This is especially important for the basement surface because it

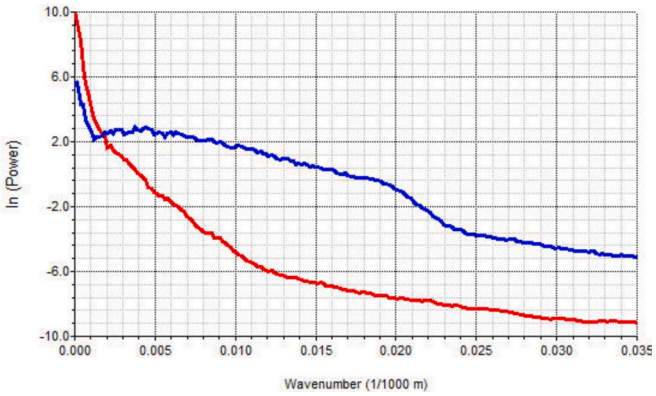

Fig. 3. Power spectrum plots from 3D calculated anomalies over North America created by the base crust inversion (red profile), and anomalies created by the basement inversion (blue profile). (For interpretation of the references to colour in this figure legend, the reader is referred to the web version of this article.)

is relatively shallow and will be subject to the greatest modification by inverse modeling.

Global models that incorporate density variations in crystalline crust and mantle layers, such as LithoRef18 (Afonso et al., 2019), WINTERC-G (Fullea et al., 2021), and ECM1 (Mooney et al., 2023) include elements of CRUST 1.0 and CRUST 2.0 and have similar regional density trends and distributions that can be correlated with the CRUST models, but there are also conflicting density patterns between models. In light of these varied crustal layer density schemes, we build first-order 3D models with six layers separated by five global horizons, respectively: 1) ETOPO1 is a 1′ x 1′ grid of topography (Amante and Eakins, 2009); 2) ETOPO1 top of ice (polar models only); 3) a zero-elevation ocean surface (note that software requirements dictate that all horizons must span entire modeled areas, therefore the top of ice and ocean surfaces are draped over topography such that the ice layer is zero thickness everywhere except over large portions in the Arctic and Antarctic, and the water layer thickness is zero above sea level); 4) base of sedimentary rock layer, or basement, which is created by subtracting ECM1 total sedimentary thickness from topography in the initial models (Mooney et al., 2023); and 5) estimated base of crust, which is calculated from Airy isostatic principles in the initial models (Blakely, 1995; Watts, 2001).

Our two-step gravity inversion method has been successfully applied in the west Texas Permian Basin (Zhang et al., 2021), in the Gulf of Mexico (Lin, 2018; Lin et al., 2019; Liu, 2021), on both flanks of the Central Atlantic Ocean (Dowla, 2019), for the conjugate eastern Africa and Antarctica continental margins (Nguyen, 2015; Nguyen et al., 2016), and in six passive margin basins along the east coast of Brazil: Barreirinhas, Ceara, Sergipe-Alagoas, Camumu-Almeda, Campos, and Santos Basins (Loureiro, 2017; Lunn, 2019; Romito, 2021; Zhang, 2021). The first structural inversion adjusts the base of crust by inverse modeling of long wavelength regional gravity anomalies. The second structural inversion adjusts basement depths that produce shorter gravity anomaly wavelengths.

To illustrate anomaly wavelengths produced by the inversions, we apply our workflow to a test area that covers most of North America (Mexico and contiguous USA). Details of this test are included in Supplementary Information (SI-2). Three gravity fields are calculated: 1) initial, before inversions, 2) after the first inversion of the base crust surface, and 3) after the second inversion of the basement. When the second calculated field (first inversion results) is subtracted from the initial field (before inversion), we obtain the gravity field produced by inverting the base of crust. And, when we subtract the third calculated field (second inversion results) from the second calculated field (first inversion results), we obtain the gravity field produced by inverting the basement. Fig. 3 is a power spectrum plot of gravity fields produced by base crust (red) and basement inversions (blue). The base crust inversion is dominated by longest wavelengths, and the basement inversion is dominated by shorter wavelengths.

Our objective is to produce a reliable sediment thickness layer, and we accept inaccuracies in estimated base of crust caused by upper mantle density anomalies, because this deep horizon is modeled in service of our objective.

3.1. Isostatic base of crust estimates

The grid cell spacings in models CRUST 1.0 (one degree) or CRUST 2.0 (two degrees) models are too large to effectively capture many sedimentary basins. Therefore, a high-resolution, idealized base of crust (or "isostatic base of crust") is calculated for the initial regional models derived from ETOPO1 elevations, a standard density contrast of 0.4 g/cm^3 at the base of the crust, and beneath a load of two or three layers: two layers above sea level (sedimentary and crystalline crust rocks), and three layers below sea level (water over sedimentary and crystalline crust rocks). The base of crust in the initial models is calculated following an Airy isostatic equation (Blakely, 1995; Watts, 2001):

$$\boldsymbol{d_{iso}} = \boldsymbol{h}\left(\frac{\rho_{av}}{\Delta\rho}\right) + \boldsymbol{d_{bar}} \tag{1}$$

where $\mathbf{d_{iso}}$ is isostatic base of crust (km), $\mathbf{h}$ is elevation (km), $\mathbf{\Delta\rho}$ is the density contrast at the base of the crust (0.4 g/cm^3), and $\mathbf{d_{bar}}$ is the isobaric crustal depth beneath the coastline (32 km assumed here); $\mathbf{\rho_{av}}$ is the average crustal density, or the load (g/cm^3); which is calculated as the sum of individual water, sediment, and crust thicknesses each multiplied by their respective densities, then divided by the total crust thickness.

Note that Eq. (1) would create crustal roots beneath seafloor spreading centers because they are topographically elevated by hot and buoyant mantle upwellings; that is, the crust has not yet reached isostatic equilibrium. We solve this problem by associating isostatic compensation with seafloor subsidence, and by adjusting our isostatic crustal thickness calculation using Stein and Stein's (1992) ocean floor subsidence formula, Eq. (2), as a proxy to scale the base of crust ($\mathbf{d_{iso}}$) as a function of lithospheric age (Müller et al., 2008). For example, ages between 100 ($\mathbf{t_2}$) and 0 Ma ($\mathbf{t_1}$) correspond to 5.5 and 2.6 km depths, respectively:

$$\begin{aligned} d_{sf} &= 2600 + 365t^{1/2}t < 20\ \text{Ma} \\ &= 5651 - 2473e^{-0.0278t}t \geq 20\ \text{Ma} \end{aligned} \tag{2}$$

where $\mathbf{d_{sf}}$ is depth of the sea floor (meters below sea level), and $\mathbf{t}$ is age (Ma).

Theoretically, lithospheric thickness at oceanic spreading centers is zero as new lithosphere is being created at that location. However, measured ridge segment crust thicknesses range from 6 km to over 7 km in the Central Atlantic and East Pacific Rise (Grevemeyer et al., 1998; Hooft et al., 2000). We compromise by adding 1.4 km to the zero-age depth of 2.6 km ($\mathbf{t_1}$ above), setting an initial base crust depth of 4 km beneath seafloor spreading centers for our scaling calculations ($\mathbf{d_0}$). An examination of global seismic refraction measurements from oceanic abyssal depths (> 3 km), and older than 100 Ma, indicates a mean Moho depth of 12.8 km (Mooney, 2015; Mooney et al., 2023). For our initial regional models, Eq. (3) linearly interpolates scaled base of crust as a function of lithospheric age ($\mathbf{t}$),for example:

$$\frac{\boldsymbol{d_{iso}}(\boldsymbol{t_2}) - \boldsymbol{d_{siso}}(\boldsymbol{t})}{\boldsymbol{d_{sf}}(\boldsymbol{t_2}) - \boldsymbol{d_{sf}}(\boldsymbol{t})} = \frac{\boldsymbol{d_{iso}}(\boldsymbol{t_2}) - \boldsymbol{d_0}(\boldsymbol{t_1})}{\boldsymbol{d_{sf}}(\boldsymbol{t_2}) - \boldsymbol{d_{sf}}(\boldsymbol{t_1})} \tag{3}$$

Where $\mathbf{d_0}$ is the base of crust depth at seafloor spreading centers (4 km), $\mathbf{d_{iso}}$ is the initial base of crust from Eq. (1), $\mathbf{d_{siso}}$ is depth to scaled crustal base at time $\mathbf{t}$, $\mathbf{d_{sf}}$ is depth to the sea floor from Eq. (2), $\mathbf{t_1}$ is 0 Ma, and $\mathbf{t_2}$

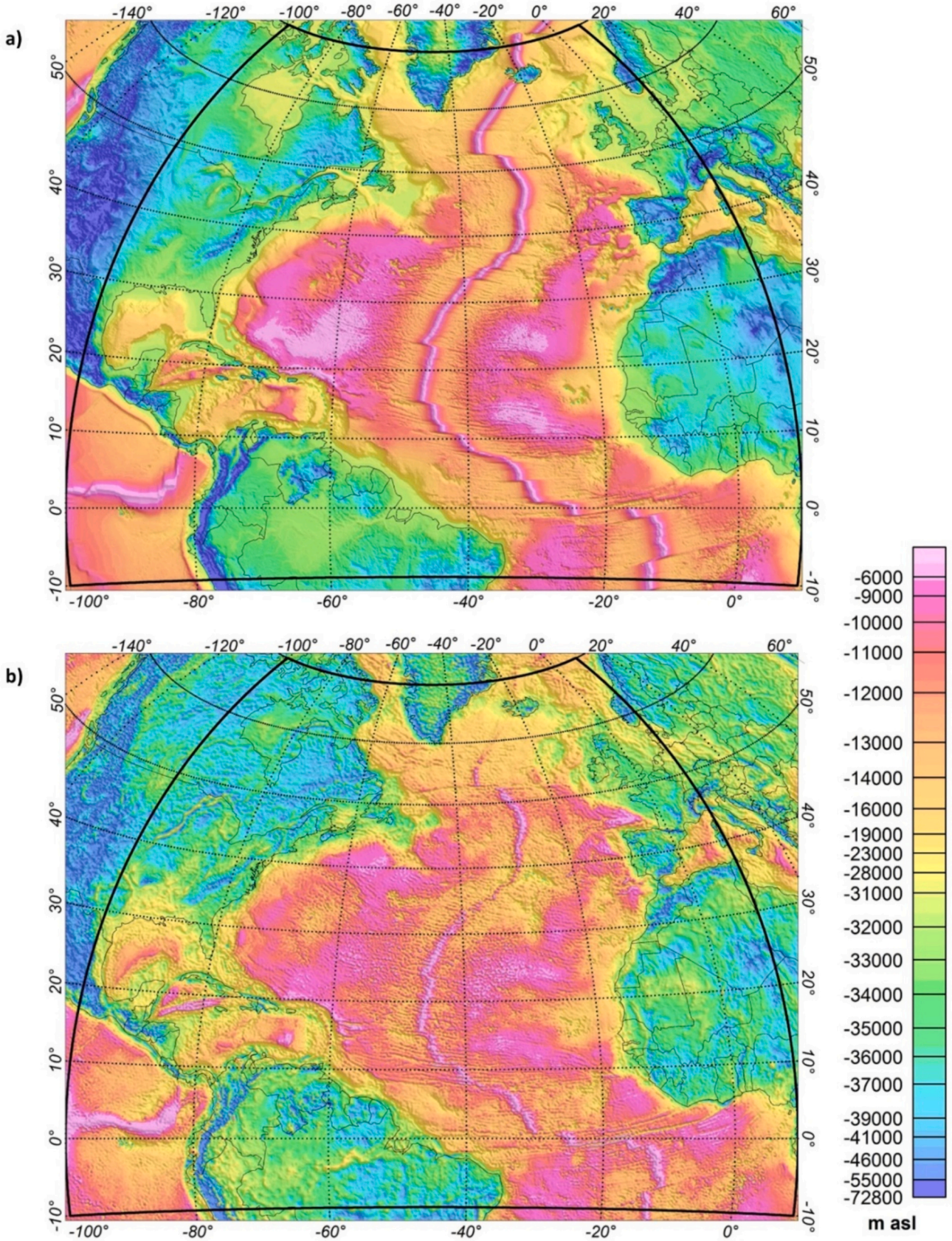

Fig. 4. Base of crust above sea level (asl) for the NW model (located in Fig. 2a); a) Initial base of crust from isostatic calculations; b) final 3D base of crust inversion from free air gravity data. The colour scale applies to both maps. The 3D base of crust inversion is used to isolate the short wavelength gravity anomalies produced by thickness variations in sedimentary basins. Inaccuracies in the base of crust correspond to regions underlain by regional upper mantle density variations. The thick latitude-longitude boundary outlines the merged overlap region of the model.

is 100 Ma.

3.2. Model densities

Four of the layers in our 3D models have constant densities: air, ice, water, and crystalline crust (0.0, 0.91, 1.026, and 2.825 g/cm^3, respectively) (Fig. 2b). Laterally varying densities are applied to sedimentary and oceanic upper mantle layers. Grid cells in modeled layer surfaces form the top and bottom of vertical prisms, each with a single density, such that adjustments during gravity inversions involve moving the boundaries of these prisms within the model.

3.2.1. Sedimentary rock layer density

Sediment layer densities are calculated from an exponential decay function that approximates sediment compaction (ranging from 2.15 to 2.7 g/cm^3) such that larger values correspond to the deeper parts of the sediment layer (Chakravarthi et al., 2013; Chakravarthi and Sundararajan, 2007; Cordell, 1973). Densities are calculated from integrations of Eq. (4) at each grid node in the models. These values are then used to create a new grid that represents density as a function of layer thickness:

$$\rho(\boldsymbol{z}) = \mathbf{2.7} - \mathbf{0.55}\boldsymbol{e}^{-2\boldsymbol{z}} \tag{4}$$

where $\boldsymbol{\rho(z)}$ is the bulk sedimentary layer density (ranges between 2.15 and 2.7 g/cm^3) and $\mathbf{z}$ is sediment layer thickness (km).

3.2.2. Upper mantle density

Upper mantle density beneath continents and oceanic regions older than ~100 Ma are 3.3 g/cm^3, but near sea floor spreading centers upper mantle densities decrease due to higher heat flow. We apply Stein and Stein's (1992) heat flow formula to scale upper mantle densities as a function of lithospheric age (Müller et al., 2008):

$$\begin{aligned} \boldsymbol{q}(\boldsymbol{t}) &= \mathbf{510}\boldsymbol{t}^{-1/2}\boldsymbol{t} \le 55\ \text{My} \\ &= \mathbf{48} + \mathbf{96}\boldsymbol{e}^{-0.0278\boldsymbol{t}}\boldsymbol{t} > 55\ \text{My} \end{aligned} \tag{5}$$

where $\mathbf{q}$ is heat flow (mW/m^2) and $\mathbf{t}$ is age (My).

We configure a linear interpolation, similar to Eq. (3) above, where $\mathbf{t_1} = 1$ Ma and $\mathbf{t_2} = 100$ Ma: $\boldsymbol{\rho_{min}} = 2.9$ g/cm^3, $\boldsymbol{\rho_{max}} = 3.3$ g/cm^3, $\mathbf{q(t_1)} =$ 510 mW/m^2, $\mathbf{q(t_2)}$ = 48 mW/m^2. Eq. (6) is used to calculate scaled upper mantle density $\boldsymbol{\rho_m(t)}$ for lithospheric age ($\mathbf{t}$), between $\mathbf{t_1}$ and $\mathbf{t_2}$, based on minimum ($\boldsymbol{\rho_{min}}$) and maximum ($\boldsymbol{\rho_{max}}$) upper mantle densities:

$$\frac{\rho_{max} - \rho_m(\boldsymbol{t})}{\rho_{max} - \rho_{min}} = \frac{\boldsymbol{q}(\boldsymbol{t_2}) - \boldsymbol{q}(\boldsymbol{t})}{\boldsymbol{q}(\boldsymbol{t_2}) - \boldsymbol{q}(\boldsymbol{t_1})} \tag{6}$$

3.3. 3D gravity inversions

Our method of gravity inversion, like many, requires data projected to a regular X-Y coordinate system (Blakely, 1995). Hence, the Earth is divided into ten regional 3D crustal models: four each around the northern and southern hemispheres, and two over polar regions (Fig. 2a). Final sediment layer thickness grids of the ten regional models are merged to create the global GST-1 model. The models are therefore constructed to overlap one another by at least 20 degrees on all sides. An examination of the north-south overlapping zone between maps NWW and NW (Fig. 2a), along longitude −90° from the equator to 60°N, indicates merge differences between 0.69% and 0.70% (Cheesman et al., 1998). Details of this analysis are included in Supplementary Information (SI-3).

Our gravity inversion method is based on the methodology of Parker (1973) and Oldenburg (1974). Inversion equations are based on Parker's (1973) landmark paper, in which he described a forward calculation method of potential fields by sums of Fourier transforms. Following this work, Oldenburg (1974) describes an iterative approach to determine geometries of potential field sources. Parker and Huestis (1974) modifies Parker's (1973) transform equations to calculate model layer thicknesses. This early work establishes a computational basis for 3D potential field modeling that is adapted into Seequent's *Oasis Montaj* algorithms.

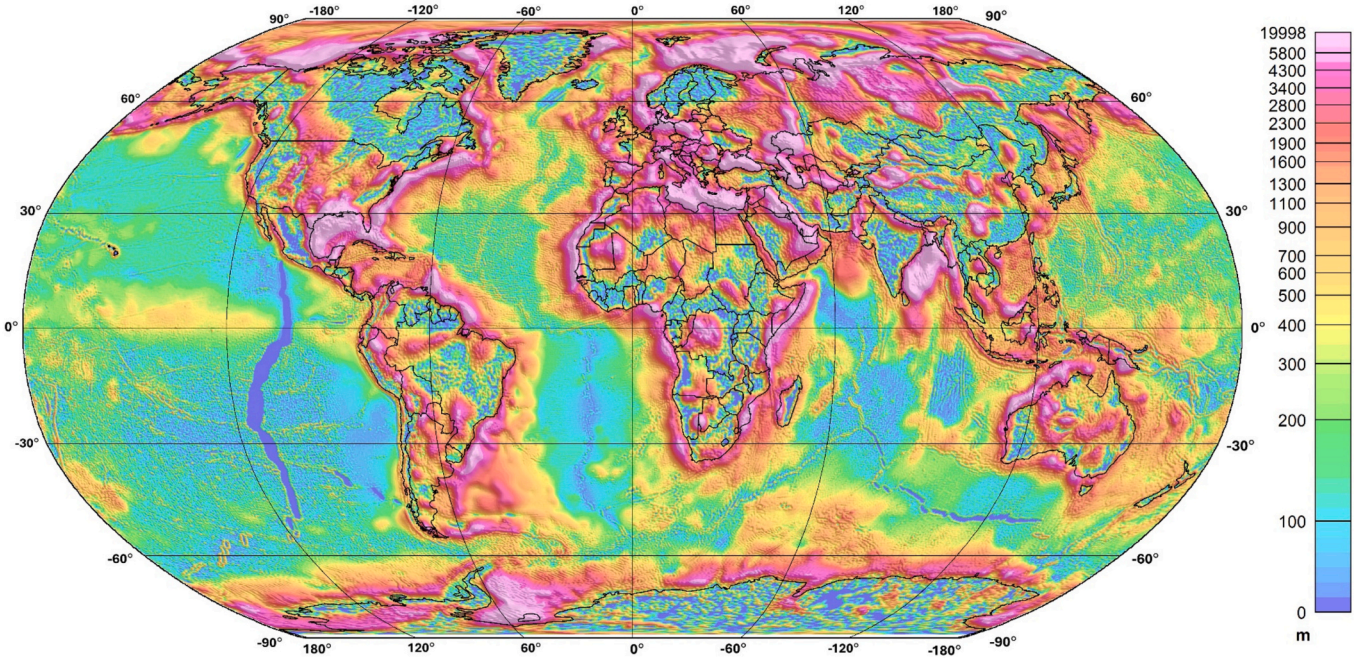

Fig. 5. Global Sediment Thickness 1 (GST-1) model calculated on a 0.125° x 0.125° grid. GST-1 modifies the total sediment thickness layer of the 1° x 1° Earth Crustal Model 1 (ECM1; Mooney et al., 2023) in 3D inversions of free air gravity anomalies. The thickest sedimentary basins are located along continental margins; deep ocean basins may have up to 300 m of sediments. Continental interiors include rift, foreland, and platform basins (see text, Section 4.1, for discussion).

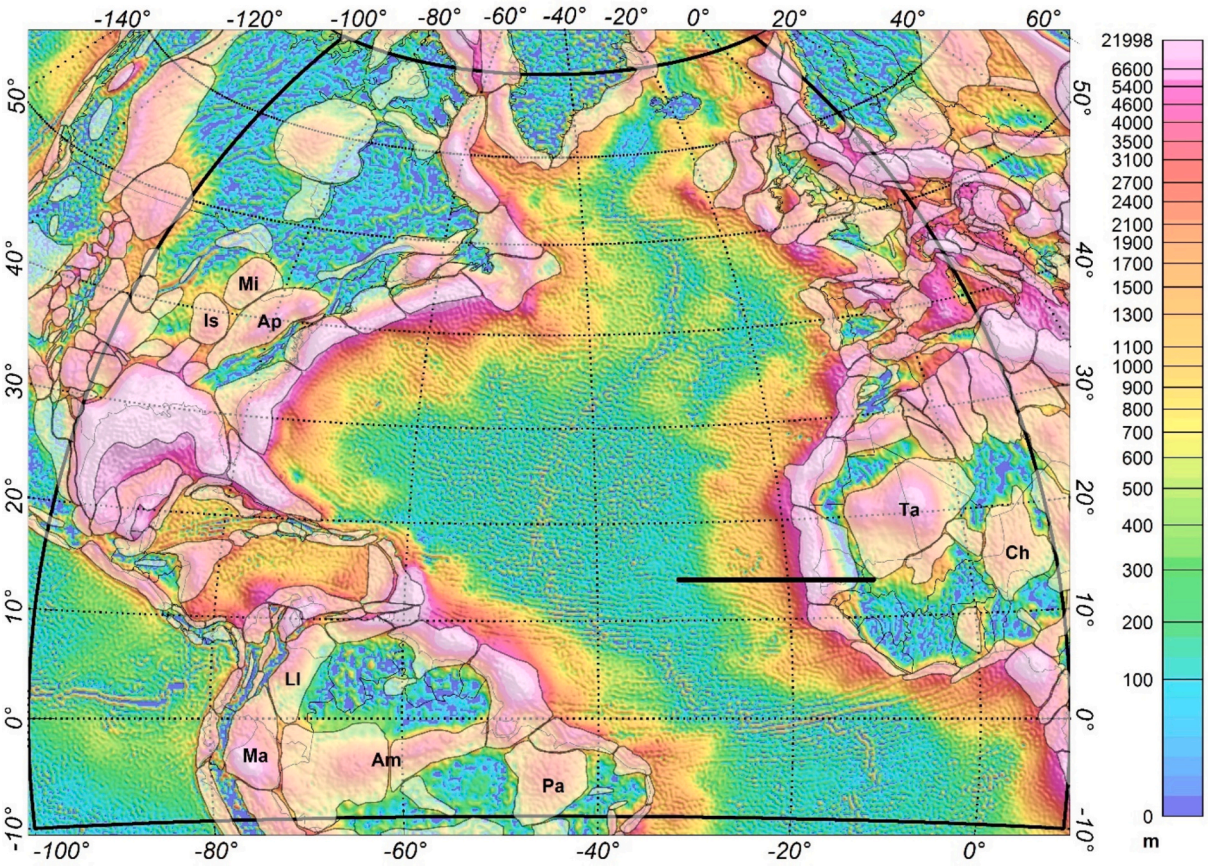

Fig. 6. Global Sediment Thickness 1 (GST-1), NW model (located in Fig. 2a). Thin black lines outline sedimentary basins (Evenick, 2021), further delimited by white semi-transparent overlays. The location of the cross section in Fig. 2b is the heavy west-east black line in western Africa. The thick latitude-longitude boundary outlines the merged overlap region of the model. Identified sedimentary basins: Appalachian (Ap), Chad (Ch), Illinois (Is), Llanos (Ll), Maranon (Ma), Michigan (Mi), Parnaiba (Pa), and Taoudeni (Ta).

Free air gravity anomaly wavelengths are transformed into spatial frequencies that can be associated with varying anomaly source depths. In our models, we consider that long wavelengths (i.e., low frequencies) correspond to lateral variations in crustal thickness and deeper (upper mantle) density variations, and that short wavelengths (i.e., high frequencies) correspond to shallow crustal features. Parker (1973) proposed a frequency-domain gravity expression:

$$F[\boldsymbol{A}(\varphi,\lambda)] = -2\pi G e^{-kz_0} \sum_{n=1}^{\infty} \frac{k^{n-1}}{n!} F[h^n] \tag{7}$$

Where **A(φ,λ)** is the long-wavelength gravity field, **G** is the universal gravitational constant, **ρ** is the crust-mantle density contrast (0.4 g/cm^3), **h** is the crustal-mantle interface depth, **k** is the modulus of the wave number field, $\mathbf{z_o}$ is the average crust-mantle interface depth and **F [A(φ,λ)]** is the two-dimensional Fourier transform.

From Eq. (7), Oldenburg (1974) proposed the iterative inversion formula (8):

$$h = F^{-1}\left[\frac{F[\boldsymbol{A}(\varphi,\lambda)]e^{kz_0}}{2\pi G\rho} + \sum_{n=2}^{n-1} \frac{k^{n-1}}{n!} F[h^n]\right] \tag{8}$$

Where $\mathbf{F^{-1}}$ is the two-dimensional Fourier inverse transform. The interface depth, base of crust or basement, controls the range of gravity wavelengths that drive the inversions, where density contrasts are 0.4 g/cm^3 or at least 0.2 g/cm^3, respectively.

The inversion algorithm we employ allows convergence limits to be set prior to model calculations (Parker, 1973). Convergence limit values (mGal) are based on comparisons of RMS differences between grids of measured gravity data versus the grids of calculated gravity data from the models. We set the convergence limit at 5 mGal in our first structural base of crust inversion. This relatively large limit is easily achieved when modeled, because incipient adjustments of the crustal base will produce RMS anomaly differences that tend to fall below the 5 mGal limit. Thus, we accomplish our goal in this first inversion to make base of crust adjustments related primarily to long wavelength gravity anomalies. Regional Model NW is an example of our base of crust inversions (Fig. 4). Our inverted crustal base for all ten regional models is consistent with ECM1 Moho depths with an average difference that ranges from +3.3 to −4.2 km. We set the convergence limit for the basement inversion at 1 mGal. This smaller limit requires greater adjustments of the shallower basement surface to produce RMS anomaly differences that fall within the 1 mGal limit. Therefore, basin geometries are improved.

4. Results

The maximum sediment thickness in model GST-1 is 20 km (Fig. 5). GST-1 basin boundaries correlate well with independently defined outlines of Earth's sedimentary basins (Fig. 6; Evenick, 2021). However, GST-1 sediment thickness values greater than 2 km extend outboard of Atlantic Ocean passive margins, such that some marginal basins in model GST-1 are larger than suggested by Evenick (2021) (Fig. 6). Excluding areas where the GST-1 sediment layer thickness is thin (~1 km) to zero (Fig. 6, colors green to blue), basin outlines over land areas follow sedimentary basin extents well (Evenick, 2021) (Fig. 6, colors yellow to magenta). For example, basin edges accurately track around the Appalachian, Michigan, and Illinois basins in North America;

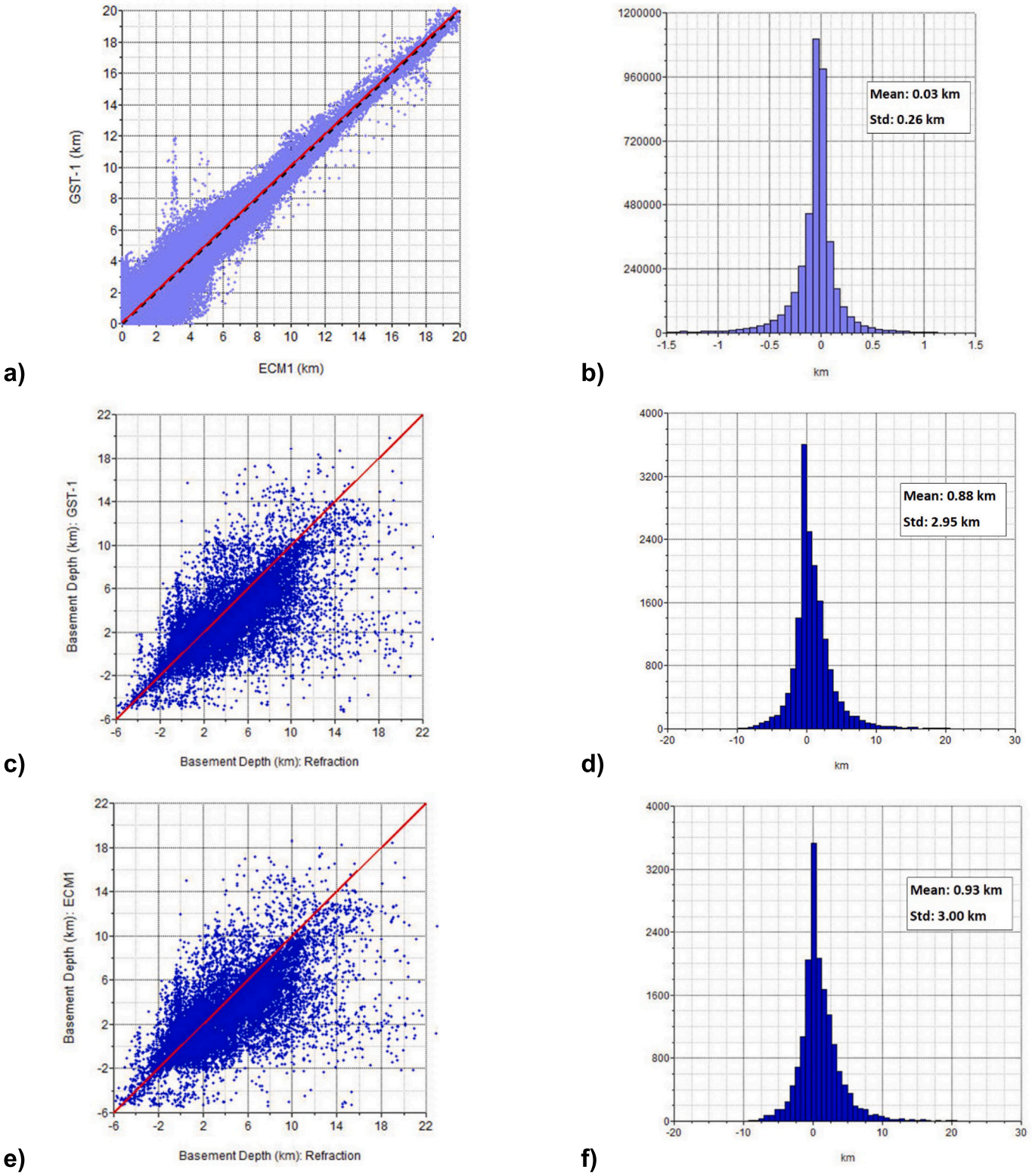

Fig. 7. Sediment thickness and basement cross plots. a) cross plot of GST-1 and ECM1 sediment thickness models; b) histogram of the difference between sediment thickness models, respective mean and standard deviation are 0.03 km and 0.26 km (1.2% of total ECM1 sediment thickness range of 20.82 km); c) and e) respective cross plots of inverted GST-1 and ECM1 basement grids and seismic refraction basement depths; and d) and f) are corresponding histograms of the basement cross plots. Respective means and standard deviations of differences between the models and seismic refraction basement are 0.88 km and 2.95 km (GST-1), and 0.93 km and 3.00 km (ECM1), which are 10.2% and 10.4% of the total seismic basement range, respectively. Red lines track one-to-one correlations. (For interpretation of the references to colour in this figure legend, the reader is referred to the web version of this article.)

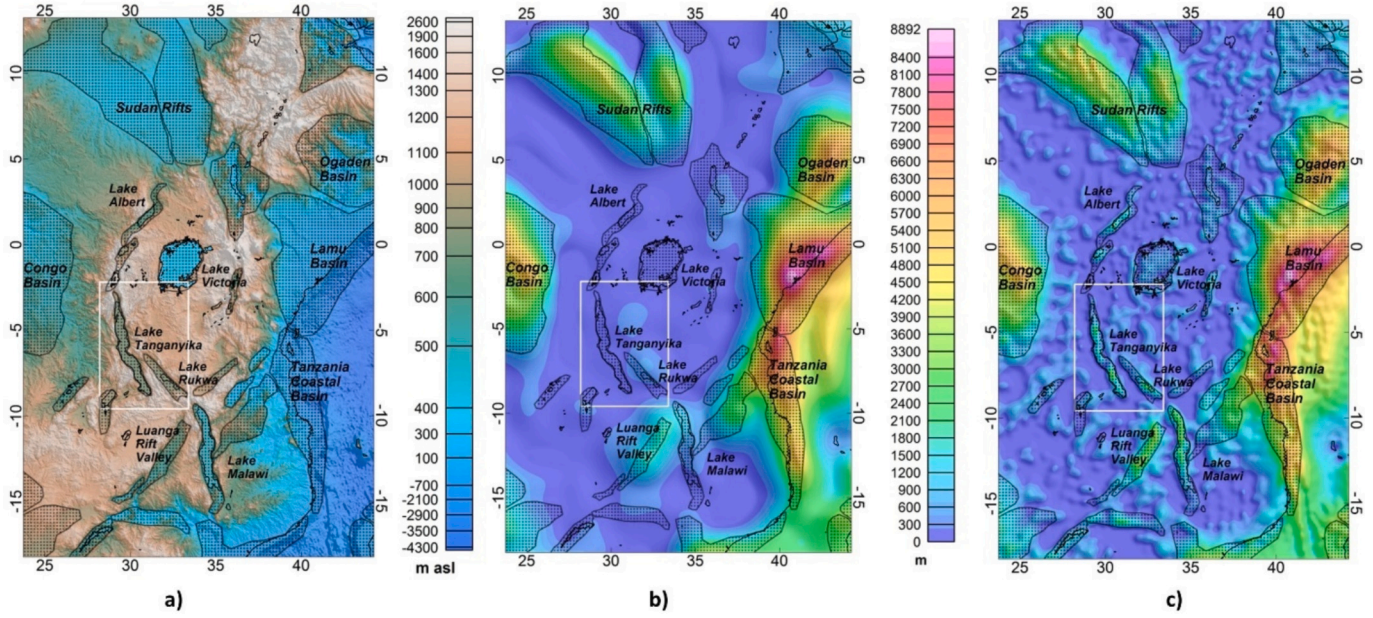

Fig. 8. East Africa topography and sediment thickness grids overlain by Evenick (2021) sedimentary basin outlines (stippled areas): a) topography, b) ECM1, and c) GST-1. Sediment thickness maps use the same colour scale. The white box is the mapped area in Fig. 15. Map outline in Fig. 1.

Maranon, Llanos, Amazon, and Parnaiba basins in South America; and the Taoudeni and Chad basins in Africa (Fig. 6).

We evaluate the accuracy of our results by direct comparisons of GST-1 with the ECM1 sediment thickness models, and by comparing basement identified from seismic refraction data (Mooney, 2015; Mooney et al., 2023) with GST-1 and ECM1 basement horizons (Fig. 7). Cross plots illustrate correlations between the sedimentary thickness models, and modeled basement with basement identified from seismic refraction data (Fig. 7a, c, and e). P-wave velocities in continental and oceanic basement are selected from seismic refraction data (Mooney, 2015; Mooney et al., 2023) with velocity for continental and oceanic basement ranging from 5.6 to 6.4 km/s and from 4.6 to 5.3 km/s, respectively (Christensen and Mooney, 1995; Mooney, 2015; White et al., 1992). A histogram graph of the difference between GST-1 and ECM1 sediment thickness models (Fig. 6b) reveals a small overall difference between the models (1.2%). We interpret GST-1 thickness variability about the one-to-one correlation line to reflect improved basin geometries produced by the basement inversions. Our modeling scheme, data coverage, and grid sampling generate more accurate and refined basement configurations, especially in smaller and shallower basins. Histograms of the difference between basement models and seismic refraction basement indicate 10.2% to 10.4% accuracy for both GST-1 and ECM1 basement models, which are within the expected accuracy of refraction data (Christensen and Mooney, 1995).

A side-by-side comparison of sediment thicknesses in eastern Africa reveals a probable limit to thickness calculations (Fig. 8). GST-1 sediment thicknesses in narrow East African rift basins align accurately with their outlines as mapped by Evenick (2021) from Lake Albert southward to Lake Malawi and the Luanga rift valley (Fig. 8), however sediment thickness in these narrow rifts is only slightly greater than the light-to-dark blue, patchy pattern that blankets GST-1. Although this subtle pattern may indeed represent individual sediment accumulations, overall sediment thicknesses due to this effect are only slightly smaller than those in the narrow East African rifts, albeit rift geometries are more coherent in this example. We further note that the patchy wavelengths are similar to the narrow rift wavelengths, indicating that an attempt to remove this effect by wavelength filtering would also remove the narrow rift basins.

4.1. Basin Types

Classifications of sedimentary basins predate the general acceptance of plate tectonic theory (Weeks, 1952). However, since the advent of plate tectonics most sedimentary basins have been categorized in terms of their tectonic setting (Bally and Snelson, 1980; Dickinson, 1974; Evenick, 2021; Frisch et al., 2011; Ingersoll, 2012; Kingston et al., 1983; Stüwe, 2007). From these proposed classifications, and considering tectonic forces that create sedimentary basins, we adapt five primary types of basins for our analysis: 1) platform basins (also called cratonic, intra-cratonic, or crustal sag basins), 2) rift basins, 3) passive margin basins, 4) forearc basins, and 5) foreland basins.

Geometrically and stratigraphically, platform basins are relatively uncomplicated. They typically form in stable continental interiors and are circular to oval shaped with diameters of about 300 to 600 km (Armitage and Allen, 2010). Platform basins are commonly filled with up to ~3 km of nearly horizontal depositional layers. Post deposition structuring and deformation may occur such as in the platform basin example below (Fig. 9) (Peterson and MacCary, 1987). However, there is no consensus for the origin and evolution of platform basins (Hartley and Allen, 1994). Klein and deV. (1995) reports that eleven hypotheses have been proposed for their origin. These hypotheses fall into groups that require continental stretching or buckling, thermal anomalies, intrusions of dense rocks into the crust, or phase changes in deep crust and upper mantle rocks (Allen and Armitage, 2012; Klein and deV., 1995).

Rift basins are endmember basins of the supercontinent cycle, also called the Wilson Cycle, that are produced by divergent tectonic forces (Bradley, 2011; Burke, 2011; Evans et al., 2016; Grenholm and Schersten, 2015; Murphy and Nance, 2013; Nance et al., 2014). The two phases of the supercontinent cycle are driven by divergent and convergent geodynamic forces. Rift basins are commonly several hundred km in length and tens of km in width, and they may be filled with up to eight km of sedimentary rocks (Chorowicz, 2005; Grauch and Connell, 2013; Peters and van Balen, 2007; Rüpke et al., 2008; Withjack et al., 2002). Structurally, rift basins are dominated by one or two large basin-bounding faults on either side of the rift. Volcanism, particularly mafic, is often associated with rift basins. Passive margin basins form along continental margins, after divergent forces have produced an ocean basin, where thick sediment layers are typically draped over continental to oceanic crustal boundaries, (O'Grady et al., 2000;

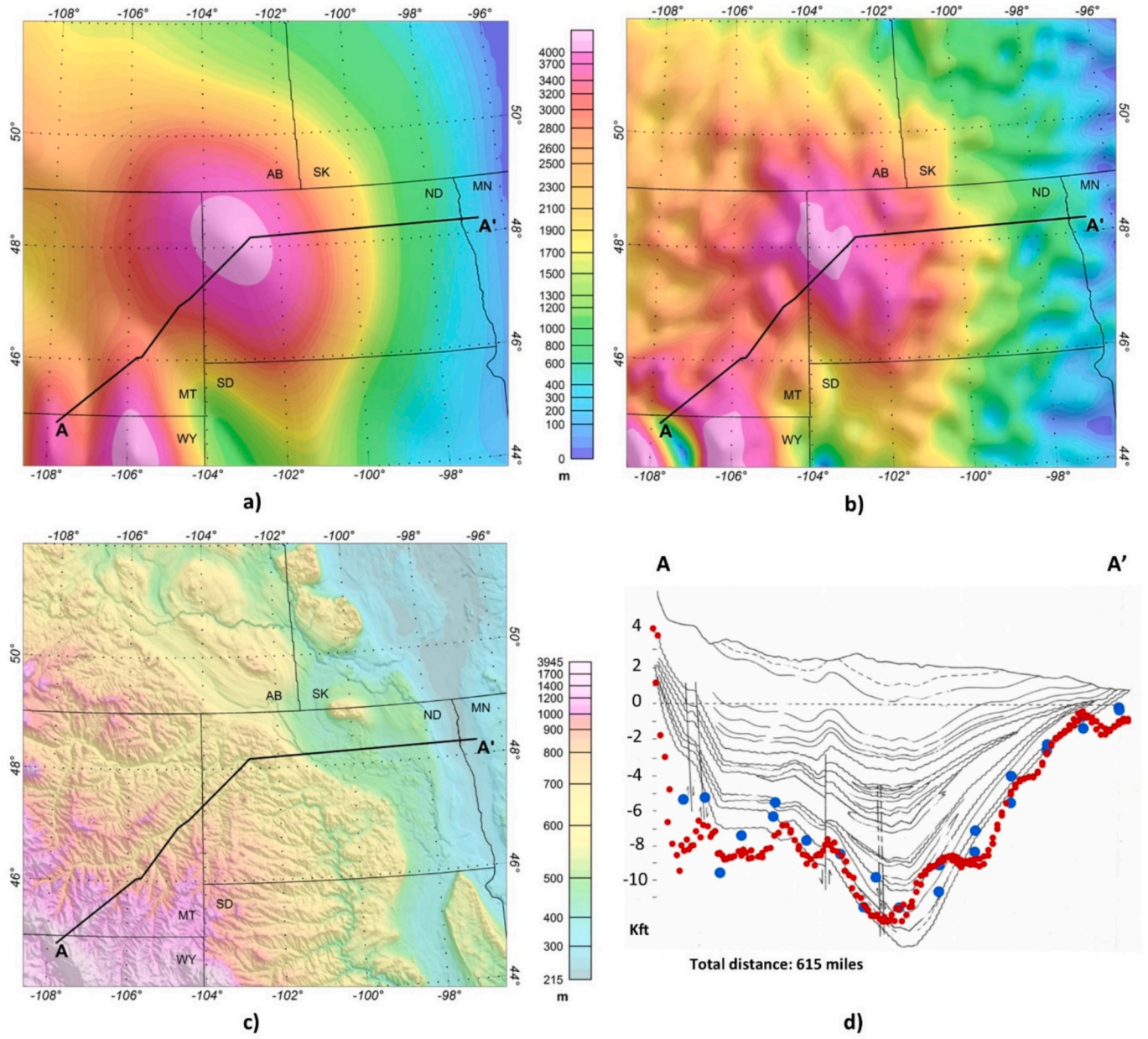

Fig. 9. Williston platform basin and cross section location: a) sediment thickness model ECM1, b) sediment thickness model GST-1. Sediment thickness maps use the same colour scale. (c) topography; and d) geologic cross section A-A', y-axis is elevations in kft above sea level (modified after Peterson and MacCary, 1987). Model ECM1 sediment thickness values are projected onto cross section A-A' with blue dots; model GST-1 sediment thickness values are indicated with red dots. The mean difference between the geologic cross section and GST-1 is −42 m with a standard deviation (SD) of 720 m (see text, Section 4.2.1, for discussion). Map area outline in Fig. 1. (For interpretation of the references to colour in this figure legend, the reader is referred to the web version of this article.)

Osmundsen and Redfield, 2011; Watts, 2012). These basins contain the thickest accumulations of sedimentary rocks, ranging from about 10 km to over 18 km, and they may extend for thousands of kilometers along continental margins (Alvey et al., 2008; Bird et al., 2005; France-Lanord et al., 1993). Passive margin basins can develop over crust that has been thickened by mantle plume sources (magmatic margins) or regions that are magma starved (amagmatic margins); and, depending on climate and basin geometry, they may be dominated by salt or carbonate deposition (Buck, 2017; Chen et al., 2013; Galloway, 2008; Harris et al., 1985; Kusznir and Karner, 2007; Scheck-Wenderoth et al., 2008; Sutra and Manatschal, 2012; Tugend et al., 2020).

Convergent forces during the second phase of the supercontinent cycle produce basins along oceanic-continental subduction zones, or collision zones between two continents, such as forearc and foreland basins (DeCelles, 2012; Roure, 2014; Watts, 1992). Forearc basins develop seaward of continental arcs over subducting oceanic lithosphere, but landward of accretionary prisms and subduction trench sediments (Noda, 2016). That is, they sit on the seaward edge of continental crust overriding subducting oceanic crust. They are generally shallow basins (a few km), but their depths and extents are controlled by relationships between tectonic plate convergence velocity and the volume of sedimentary rocks eroded from the continent and deposited into the forearc (Noda, 2016). Foreland basins, also called retro-foreland basins, develop landward of continental arcs. They are typically asymmetrical in shape, where the deepest part of the basin, sometimes exceeding seven km, is close to the arc with the basin then gradually thinning away from the arc (Allen et al., 1986; Calderon, 2018; DeCelles and Giles, 1996; Fritz and Mitchell, 2021; Pratsch, 1986; Tufano and

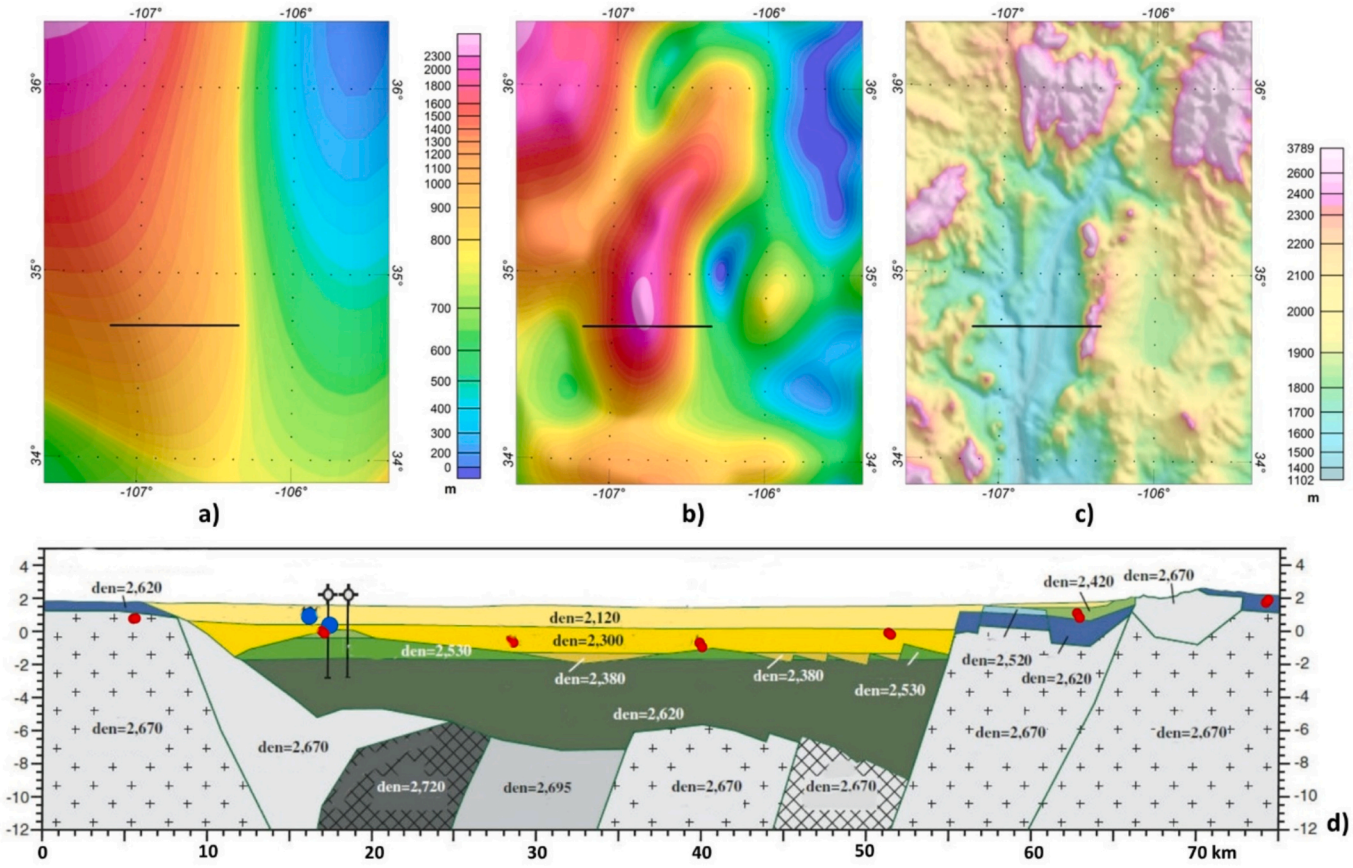

Fig. 10. Rio Grande rift basin and cross section location. a) sediment thickness model ECM1, b) sediment thickness model GST-1. Sediment thickness maps use the same colour scale. (c) topography; and d) geologic cross section (modified after Grauch and Connell, 2013). Projected ECM1 grid nodes are large blue dots and GST-1 grid nodes are small red dots. Cross section density and depth units are kg/m^3 and km asl, respectively. The mean difference between the top of the high-density sedimentary layer in the cross section and GST-1 is 937 m, with a SD of 796 m (see text, Section 4.2.2, for discussion). Map area outline in Fig. 1. (For interpretation of the references to colour in this figure legend, the reader is referred to the web version of this article.)

Pietras, 2017).

To further evaluate the validity of model GST-1, we compare depth plots of inverted GST-1 basement (beneath GST-1 sediment thickness) and ECM1 top of upper crystalline crust layer (basement. Beneath ECM1 sediment thickness) on published cross sections. We select sedimentary basins corresponding to the five basin types described above (Allen et al., 2015; Bally and Snelson, 1980; Dickinson, 1974; Ingersoll, 2012; Kingston et al., 1983): platform basins, rift basins, passive margin basins, forearc basins, and foreland basins. Plotted basement depth values of models GST-1 and ECM1 illustrate the increased resolution of model GST-1.

4.2. Basin geometry comparisons

Side-by-side comparisons (Figs. 9–14) reveal the relatively smooth ECM1 total sediment thickness layer compared to the more detailed GST-1 model, which is due to the differing grid cells spacings of ECM1 and GST-1(1.0° and 0.125°, respectively). Note also that these different grid cell increments are also the computational increments used to build the sediment thickness models. For each example of a basin cross section displayed below, the nearest grid node values from each sedimentary thickness model are converted to basement depths and projected onto the cross section. That is, any model grid node that falls within 1.0° or 0.125° along an example cross section is projected into the cross section from ECM1 and GST-1 models, respectively. Thus, modeled values of sedimentary thickness (as basement depths) are compared directly to published basin cross sections.

4.2.1. Williston platform basin, United States and Canada

The Williston Basin is a platform basin that straddles the border between the United States and Canada, spanning parts of Montana, North Dakota, Saskatchewan, and Manitoba (Fig. 9). It is oval shaped and contains more than 10 kft (~3 km) of Cambrian to Tertiary sediment thickness that exceeds 10 kft (Peterson and MacCary, 1987). The size and shape of the Williston basin is clear by comparing sedimentary thickness models (Fig. 9a and b). The basin was mildly deformed by Laramide-age (ca. 70–40 Ma) compressional forces, indicated by recent anticlines evident in the cross section (Fig. 9d). ECM1 grid nodes (sediment thickness values) within 1° distance from the cross section are projected onto the cross section and plotted as large blue dots. GST-1 grid nodes within 0.125° distance from the cross section are projected onto the cross section and plotted as smaller red dots. Both sets of projected grid nodes are consistent with the shape of the basin, however GST-1 grid nodes show more detail and correlate with interpreted cross section structuring.

4.2.2. Rio Grande rift basin, United States

The Rio Grande basin is a north-south oriented rift basin in New Mexico and Colorado, southwest United States (Fig. 10). It is filled with Oligocene through Pleistocene sediments with a maximum thickness of just over 4270 m (Grauch and Connell, 2013). Grauch and Connell (2013) generated 2D and 3D models of the Rio Grande rift basin to test conflicting interpretations of its structure and evolution. ECM1 shows no expression of the basin, while GST-1 depicts an elongated shaped sedimentary thickness that coincides with the basin topography (Fig. 10a-c). ECM1 and GST-1 grid node values are projected onto cross section C-C′

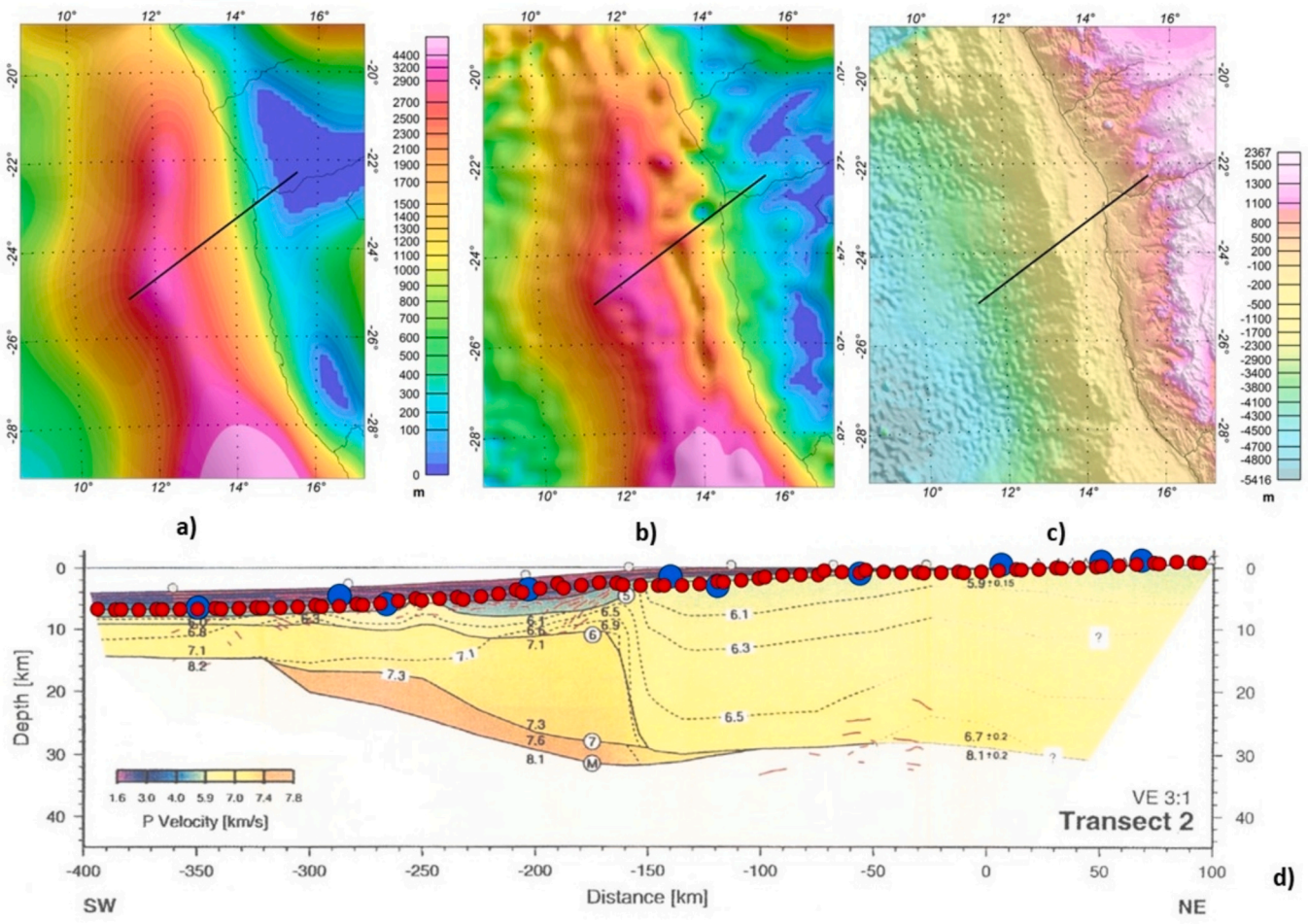

Fig. 11. Cape passive margin basin and cross section location. (a) Sediment thickness model ECM1, (b) sediment thickness model GST-1. Sediment thickness maps use the same colour scale. (c) topography; and (d) geologic cross section (modified after Bauer et al., 2000). Model ECM1 sediment thickness values are projected onto cross section A-A' with blue dots; model GST-1 sediment thickness values are indicated with red dots. The mean difference between the geologic cross section and GST-1 is −2590 m with a SD of 2373 m (see text, Section 4.2.3, for discussion). Map area outline in Fig. 1. (For interpretation of the references to colour in this figure legend, the reader is referred to the web version of this article.)

(Fig. 10d) (Grauch and Connell, 2013). Due to the location of the cross section, only two grid nodes from ECM1 can be plotted (from 35°N, 107°W and 34°N, 107°W, north and south of the cross section). ECM1 grid nodes plot above sea level while GST-1 grid nodes plot at greater depths, however GST-1 depths do not coincide with the basement depth modeled by Grauch and Connell (2013) (Fig. 10d). The density of the deepest sedimentary layer in their model is 2.62 g/cm^3, which is relatively high for sedimentary rocks and nearly as high as the modeled crystalline crust density below (2.67 g/cm^3). This small density contrast may have contributed to the shallower GST-1 calculated basement inversion depths.

4.2.3. *Cape passive margin basin, Namibia*

The Cape Basin is a segment of the western Africa sub-Saharan passive margin located on the central coast of Namibia (Fig. 11) (Bauer et al., 2000). It is bounded on the north by the Walvis Ridge, a volcanic edifice produced by the Tristan da Cunha mantle plume as the South Atlantic opened (~130 Ma) (Bird and Hall, 2016). ECM1 incorporates the GlobSed model (Straume et al., 2019), which is an updated sediment thickness model of the world's oceans, and the accuracy of this model may explain the close correlation between ECM1 and GST-1 maps (Fig. 11a and b). Grid nodes from the sedimentary thickness models along Transect 2, a crustal-scale geologic cross section interpreted from wide-angle seismic reflection and refraction data (Bauer et al., 2000), track the general seaward slope of the basin (Fig. 11d). However, a large mismatch between projected GST-1 depths and a deep sub-basin or trough, located between −240 to −150 km along the cross section, has biased the average difference between GST-1 and the cross section (mean = −2589.6 m). We note that GST-1 has successfully modeled this trough, located subparallel to the coast roughly between 24°S and 27°S, but that the cross section is located slightly north of the modeled trough (Fig. 11b).

4.2.4. *Valparaíso forearc basin, Chile*

The western margin of South America has experienced four orogenic events since the Neoproterozoic Era: Pampean (545–520 Ma), Famatinian (616–385 Ma), Gondwanian (348–259 Ma), and Andean (190–0 Ma) (Charrier et al., 2015). Deposition in the Valparaiso Basin began during the hiatus between the Gondwaninan and Andean orogenies and continues today (Laursen et al., 2002). The difference between sedimentary models GST-1 and ECM1 is striking (Fig. 12a and b). GST-1 displays a pair of relatively thin, subparallel sedimentary subbasins that follow the coast, but ECM1 sedimentary thickness is broad and discontinuous. However, the sedimentary layer in the Valparaiso Basin is relatively thin (< 3 km) (Fig. 12d). Two ECM1 grid nodes project into the cross section, but one of them projects above the water bottom because it coincides with the southern grid node at 33°S, 77°W, and the other grid node projects in from the north at 32°S, 77°W. Although GST-

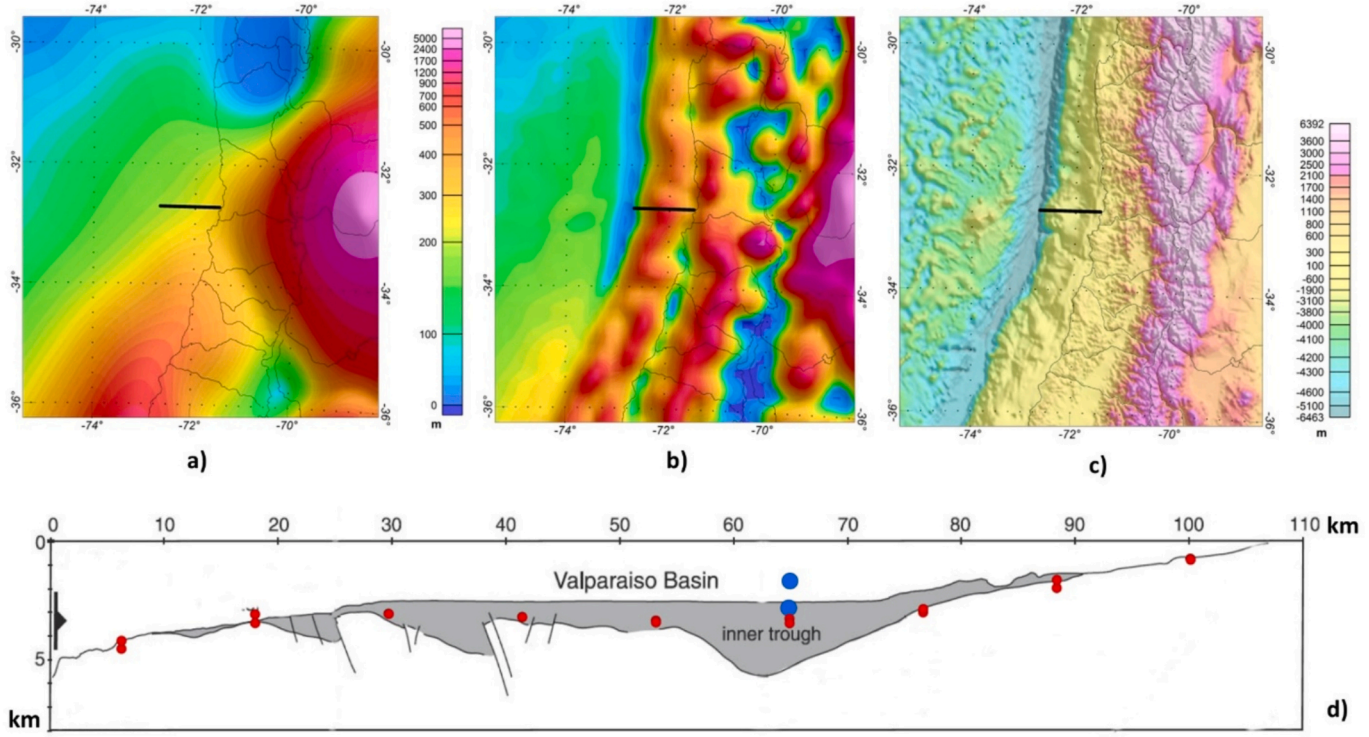

Fig. 12. Valparaiso forearc basin and cross section location. (a) Sediment thickness for model ECM1; (b) sediment thickness for model GST-1. Sediment thickness maps use the same colour scale. (c) topography; and (d) geologic cross section (modified after Laursen et al., 2002). Projected ECM1 sedimentary thickness values are large blue dots and GST-1 sediment thickness values are small red dots. The mean difference between the geologic cross section and GST-1 is 253 m with a standard deviation of 640 m (see text, Section 4.2.4, for discussion). Map area outline in Fig. 1. (For interpretation of the references to colour in this figure legend, the reader is referred to the web version of this article.)

1 grid nodes do not project to the deepest part of the basin (~63 km along the profile), they are largely consistent with the shape of the basin.

4.2.5. *Maturin foreland basin, Venezuela*

The Maturin foreland basin formed by oblique convergence between the Caribbean and South American Plates, southeast of the Serrania and Monagas thrust belts (Fig. 13) (Jacome et al., 2003). Kinematically, northeastern South America is riding over the southeastern edge of the Caribbean Plate, where the Caribbean Plate is moving due east at about 2 cm/a with respect to South America (Masy et al., 2015; Schmitz et al., 2008; Weber et al., 2001). Schmitz et al. (2008) report that the basin is filled with 8–12 km of Neogene sediments sourced from the west by the Serrania del Interior thrust belt and from the south by the Guyana Shield (outcropping Precambrian crystalline basement). GST-1 and ECM1 sediment thickness models are similar (Fig. 13a and b) with both sets of projected grid node depths tracking the shape of the Maturin Basin reasonably well southeast of basement thrusts, but they plot above the thrusts to the northwest, possibly due to higher density deep sedimentary layers (Fig. 13d-f).

5. Discussion

Our analysis includes comparisons of GST-1 results with other global models, along with caveats and limitations, that are addressed in the Supplementary Information.

5.1. *GST-1 in comparison with global models*

We quantify computed sediment thickness differences between GST-1 and three global models: 1) SGG-UGM-2 gravity models (Liang et al., 2020); 2) ECM1 crystalline crust and upper mantle layer densities (Mooney et al., 2023), and 3) LithoRef18 crystalline crust, upper mantle, and sub-450 km asthenospheric layer densities (Afonso et al., 2019). In their comparison of SGG-UGM-2 with EGM2008, Liang et al. (2020) note that large differences exist between the gravity models where measured gravity data are sparse or do not exist, such as Antarctica, the Tibetan Plateau and parts of South America and Africa. They also note that discrepancies exist along coastlines. We therefore select three large test areas to compare SGG-UGM-2 and EGM2008 gravity models, 1) North America, 2) central Africa, and 3) central and south Asia (Supplementary Information, SI-1 & SI-4).

5.1.1. *Gravity model SGG-UGM-2*

The SGG-UGM-2 global gravity grid (Liang et al., 2020) integrates GOCE, GRACE, and updated Satellite Altimetry gravity data with EGM2008 (Drinkwater et al., 2003; Sandwell et al., 2014; Tapley et al., 2004). First, we compare the two gravity models by subtracting SGG-UGM-2 from EGM2008 gravity anomalies. Differences between the two models for North America, central Africa, and central and south Asia are 0.73%, 1.26%, and 1.33%, respectively (Supplementary Information, SI-1). Next, we replace EGM2008 with SGG-UGM-2 gravity models in the test models and apply GST-1 workflow: invert base of crust, invert basement, calculated sediment thickness. Differences between GST-1 and test area sediment thicknesses for North America, Africa, and Asia are 0.56%, 0.66%, and 0.48%, respectively (Supplementary Information, SI-1).

Local differences are computed as a ratio of the calculated difference over the sum of thicknesses at each grid node, where the average summed thickness is greater than 500 m. As the summed thickness approaches zero, the local difference grows to meaningless values, therefore we limit summed thickness at 500 m. Local differences between GST-1 and test areas are −0.029%, 0.047%, and 0.516% for North America, Africa, and Asia, respectively. Local differences for summed thickness greater than 1000 m are −0.024%, −0.014%, and 0.363%,

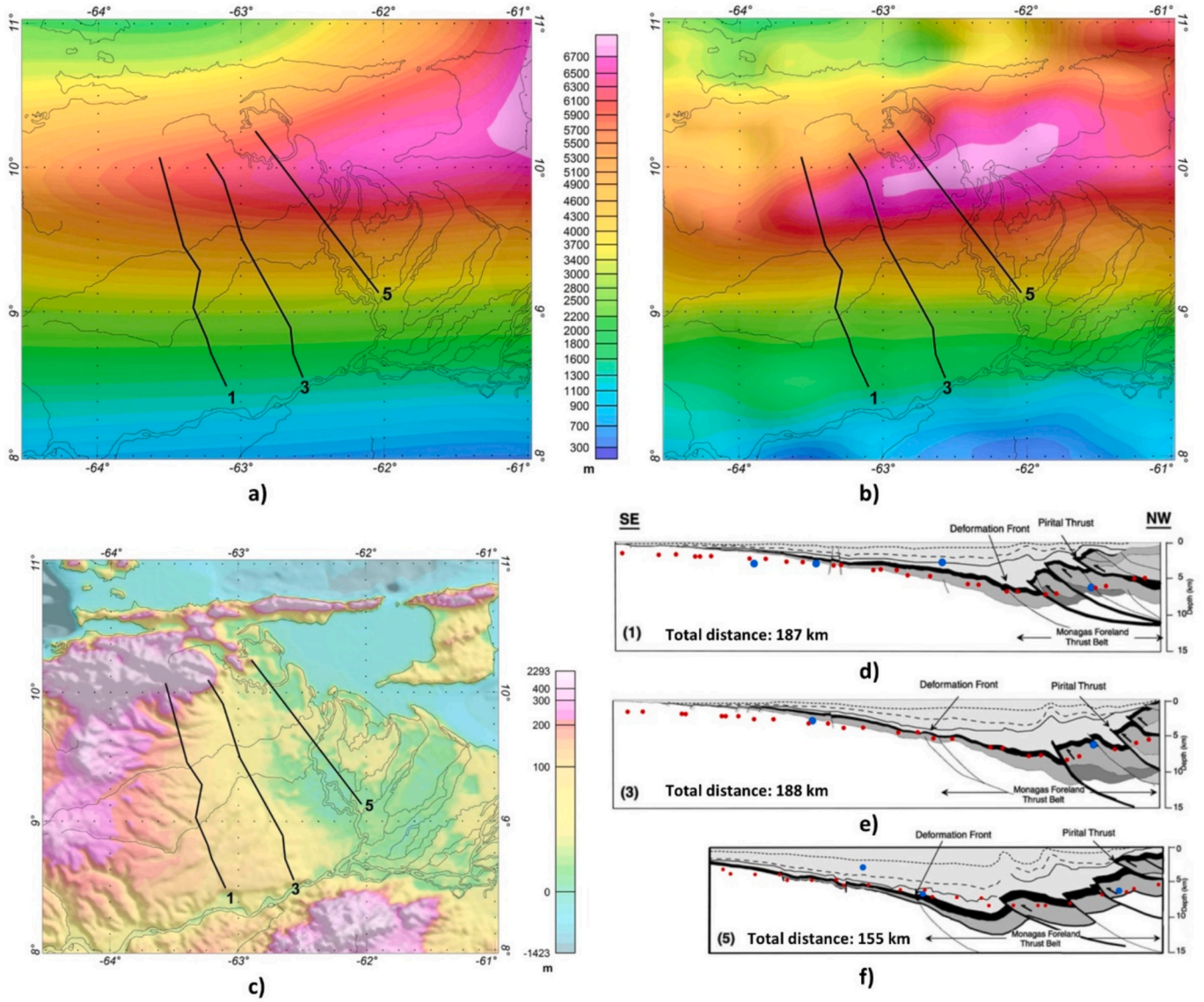

Fig. 13. Maturin foreland basin and cross section location. (a) Sediment thickness for model ECM1; (b) sediment thickness for model GST-1. Sediment thickness maps use the same colour scale. (c) topography; and d-f) geologic cross sections (modified after Jacome et al., 2003). Projected ECM1 grid nodes are large blue dots and GST-1 grid nodes are small red dots. The mean difference between the geologic cross section and GST-1 are (d) -23 m with a standard deviation (SD) of 1142 m; (e) 451 m, SD 2369 m; (f) 1062 m, SD 1633 m (see text, Section 4.2.5, for discussion). Map area outline in Fig. 1. (For interpretation of the references to colour in this figure legend, the reader is referred to the web version of this article.)

respectively (Supplementary Information, SI-1).

5.1.2. Crust and lithospheric models: ECM1 and LithoRef18

Global crust and lithospheric models, ECM1(Mooney et al., 2023) and LiithoRef18 (Afonso et al., 2019), include lateral density variations. ECM1 has three crystalline crust layers and an upper mantle layer. LithoRef18 has a single crust layer and two sub-crustal layers: lithosphere and upper asthenosphere. We replace the constant GST-1 layer density (2.825 g/cm^3) with ECM1 varying crystalline crust densities (averaging three layers) and replace GST-1 with ECM1 upper mantle densities in each of the test models. We again employ the GST-1 workflow and calculate sediment thickness differences between these test models.

Differences between GST-1 and ECM1 sediment thickness models in the three test areas are 0.71%, 0.61%, and 0.48% for North America, Africa, and Asia, respectively. Local differences for summed thickness greater than 500 m are −0.081%, 1.272%, and −2.915% for North America, Africa, and Asia, respectively. Local differences for summed thickness greater than 1000 m are −0.082%, −0.999%, and −2.071%, respectively (Supplementary Information, SI-4).

We test LithoRef18 (Afonso et al., 2019) with the same workflow and the respective differences between GST-1 for North America, Africa, and Asia are 1.52%, 0.61%, and 0.48%. Local differences for summed thickness greater than 500 m are 0.986%, −2.180%, and 2.129% for North America, Africa, and Asia, respectively. Local differences for summed thickness greater than 1000 m are 0.739%, −1.871%, and 1.166%, respectively (Supplementary Information, SI-4).

5.1.3. Density layers and density contrasts

The test results are quite similar for the two gravity models (EGM2008 and SGG-UGM-2) because the maximum difference between gravity fields is less than 1.4%. In addition, although it may seem intuitive that adding laterally varying densities to crust and lithospheric layers should produce results different from GST-1, we see that the GST-1 workflow produced nearly the same results for all three test areas, including varying densities in crystalline crust and upper mantle layers

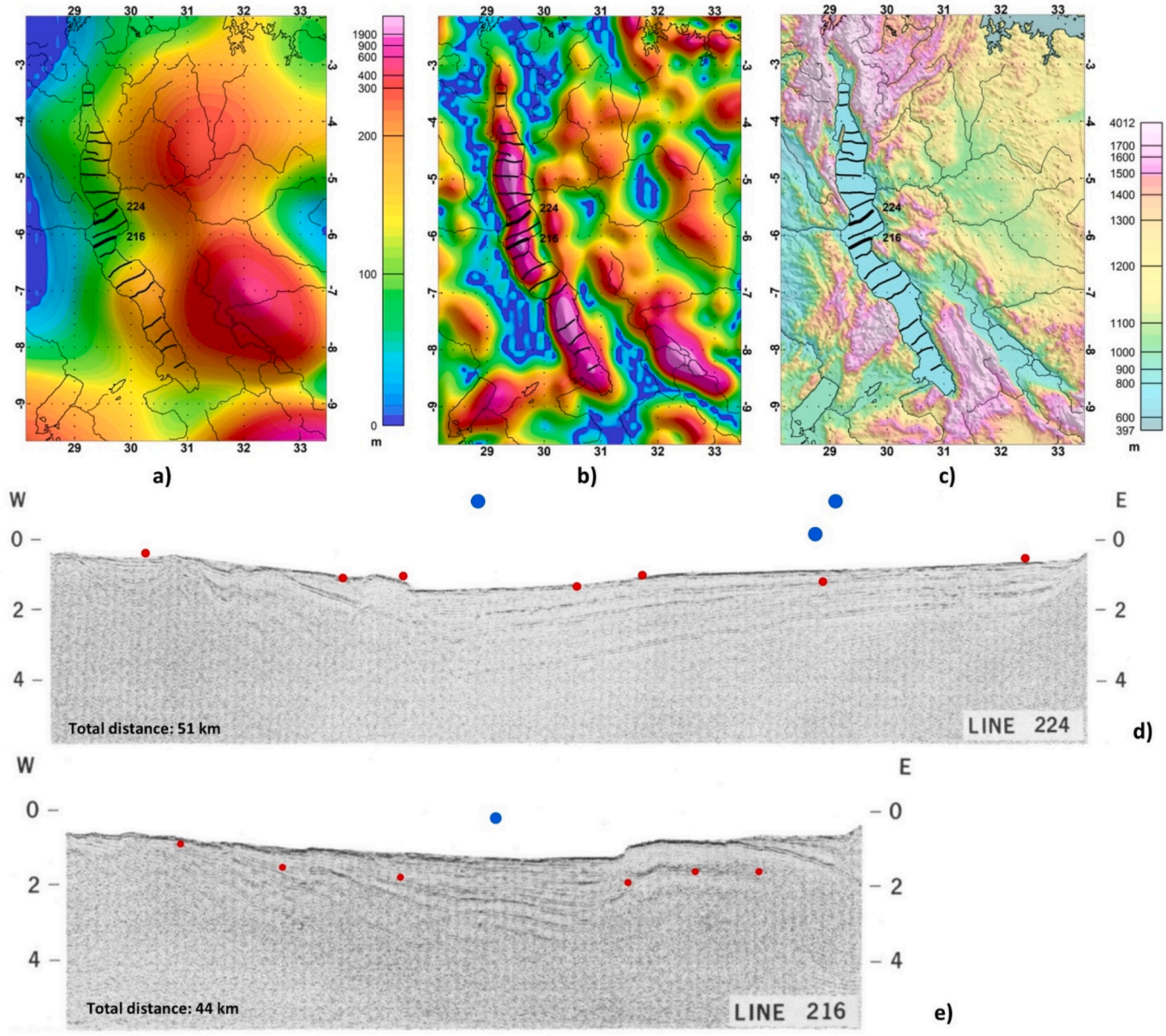

Fig. 14. Two of 21 seismic reflection sections (thick and thin black lines respectively) through Lake Tanganyika, a rift basin within the East African rift zone (Rosendahl et al., 1986). a) Sediment thickness for model ECM1; (b) sediment thickness for model GST-1. Sediment thickness maps use the same colour scale. (c) topography; and d, e) seismic section imagess. Projected ECM1 grid nodes are large blue dots and GST-1 grid nodes are small red dots. The mean difference between the base of coherent reflections in the seismic images and GST-1 are (d) 654 m, standard deviation (SD) 442 m and (e) 1864 m, SD 796 m. Map area outline in Fig. 8. (For interpretation of the references to colour in this figure legend, the reader is referred to the web version of this article.)

(Supplementary Information, SI-1). Computed sediment thickness differences range less than 1.0% with one exception (1.52%).

Over the North American test area ECM1 average crystalline crust densities (2.746 to 2.865 g/cm^3) and upper mantle densities (3.183 to 3.352 g/cm^3) have respective ranges of 0.119 and 0.169 g/cm^3 (Supplementary Information, SI-5). Over this large region (~17.5 million km^2) the average lateral density gradients in crystalline crust and upper mantle layers are small (0.07 and 0.06 g/cm^3, respectively). Therefore, density variations within layers, tied to 1° x 1° grid cells, vary far too gently to impact GST-1 gravity inversions. However, density contrasts at layer boundaries do impact gravity inversions. Respective base of crust density contrasts, at the crust-mantle boundary, for GST-1 and ECM1 models are 0.451 to 0.479 g/cm^3 and 0.448 to 0.546 g/cm^3; and respective basement density contrasts for GST-1 and ECM1 models are even larger: 0.268 to 0.682 g/cm^3 and 0.244 to 0.706 g/cm^3. Thus, GST-1 gravity inversions are driven by density contrasts at basement and base of crust layer boundaries, where density contrasts span similar ranges between both GST-1 and ECM1 models.

In the Supplementary Information section (SI-6), we map four global model crystalline crust and upper mantle densities for comparison: LithoRef18 (Afonso et al., 2019), WINTERC-G (Fullea et al., 2021), ECM1 (Mooney et al., 2023), and GST-1. Although some variations are consistent across all models, such as major seafloor spreading centers, other parts show dramatic differences. For example ECM1 and LithoRef18 show low densities in northern Africa and higher densities in southern Africa, but WINTERC-G has these trends reversed. ECM1 has an imprint of interpreted crustal types in the crust and mantle, but less so in LithoRef18 and WINTERC-G.

5.2. Dynamic topography and lithospheric flexure

In addition to density variations in crustal and mantle layers, gravity anomalies can also be produced by dynamic topography and lithospheric flexure. Flow in the mantle may cause uncompensated surface deformations known as dynamic topography (Flament et al., 2013), and the lateral strength of the lithosphere may also support uncompensated topographic relief, a process known as lithospheric flexure (Watts, 2001). Both dynamic topography and lithospheric flexure may yield topography at wavelengths on the order of 2000 km to 5000 km, and our inversion of the base of crust will be biased by these processes at long wavelengths. However, these long wavelength disturbances have a negligible effect on our modeling of sedimentary basin thickness (Colli et al., 2016).

5.3. GST-1 caveats and limitations

The ECM1 sediment thickness model (Mooney et al., 2023) is derived from seismic measurements, whereas the GST-1 model is based on seismic measurements and 3D gravity inversions. Caveats exist for both models: ECM1 velocity measurements were made over a period of decades, and they are variable in quality as well as areal sampling (Mooney et al., 2023). GST-1 inversion results are dependent on data vintage, quality, and areal sampling of the data sets that underpin the grids used in the inversions, specifically topography and gravity (Amante and Eakins, 2009; Kenyon et al., 2008; Pavlis et al., 2012; Scheinert et al., 2016).

A reasonable regional correlation exists between the ECM1 sediment thickness layer and GST-1 models, including their correlations with the geologic/geophysical cross sections (Figs. 9–13). Yet, some examples, such as the rift and forearc basins presented above (Figs. 10 and 12) illustrate that basin size may be a limiting factor in the GST-1model thickness. To further test this idea, we examine one of the narrow rift basins in the larger East African Rift zone discussed above (Fig. 8). In Lake Tanganyika (Fig. 14) we see that GST-1 solutions barely plot beneath the water bottom (Rosendahl et al., 1986), which suggests a limitation of our approach when modeling narrow rift basins.

GST-1 represents a significant improvement over existing sediment thickness maps, however local density anomalies in the sedimentary section or in the crust or upper mantle may produce artifacts. Thick salt accumulations within sedimentary layers, such as in the Gulf of Mexico or on the flanks of the Central and South Atlantic Oceans, can produce gravity anomalies on the order of tens of mGals. Our 0.125° grid resolution is generally too coarse to identify individual salt features however the aggregate effect of thick, low-density salt layers may produce gravity minima that have the effect of deepening sedimentary basins during the basement inversions. Conversely, high-density carbonate-dominated basins may result in shallower inverted basement depths. Thermal anomalies exist beneath continents in the upper mantle, such as the Afar mantle plume at the intersection of the Red Sea and the Gulf of Aden and beneath the Great Basin in western North America (Ebinger et al., 2010; Mooney and Kaban, 2010). High-temperature thermal anomalies produce low density upper mantle rocks that can approach densities of some lower crust (3.0–3.2 g/cm^3). In these cases, inversions of crust depth will compute depths that are too deep. We acknowledge the limitations of resolving narrow (<50 km) basins thicknesses, and artifacts due to local density variations within basins, crust, and upper mantle. Nevertheless, the examples presented above demonstrate a significant improvement in GST-1 over existing sedimentary thickness models.

6. Conclusions

Global Sedimentary Thickness 1 (GST-1) is a high-resolution model of the Earth's sedimentary layer defined on a 0.125° x 0.125° grid (~14 km at the equator). This model represents an eight-fold improvement in spatial resolution over the total sedimentary thickness layer in the 1° X 1° Earth Crustal Model (ECM1; Mooney et al., 2023). A cross plot of GST-1with ECM1 shows a strong correlation. Grid node values of GST-1 are in good agreement with geologic cross sections through five types of sedimentary basins: platform, rift, passive margin, forearc, and foreland.

There are limitations to the modeling approach presented here. Regarding inverse gravity models, basin depths can be refined with additional gravity data measured at closer intervals. Local density anomalies in the crust and upper mantle also present modeling challenges. Despite these limitations, model GST-1 provides significantly improved resolution of basin geometries in comparison with model ECM1. GST-1 may be used to anchor a diverse range of global, regional, or local studies where additional geological and geophysical data are available such as wells, seismic (reflection and refraction), magnetic, and higher resolution gravity. This utility spans a broad range of applications related to hydrocarbon and mineral exploration, geothermal resource evaluation, and sedimentary basin formation and evolution studies.

CRediT authorship contribution statement

Dale E. Bird: Writing – review & editing, Writing – original draft, Supervision, Project administration, Methodology, Investigation, Formal analysis, Data curation, Conceptualization. **Walter D. Mooney:** Writing – review & editing, Methodology, Investigation, Formal analysis.

Declaration of competing interest

The authors declare the following financial interests/personal relationships which may be considered as potential competing interests: (Dale E Bird reports was provided by none. Dale E. Bird reports a relationship with none that includes:. Dale E Bird has patent none pending to none. All work presented was done without any financial support whatsoever. If there are other authors, they declare that they have no known competing financial interests or personal relationships that could have appeared to influence the work reported in this paper.)

Data availability

The Global Sediment Thickness 1 (GST-1) model may be accessed at https://zenodo.org/uploads/15320474

Acknowledgements

We thank Seequent, creator of the effective *Oasis Montaj* potential fields mapping, processing, and modeling software. We have benefitted from constructive criticism from C. Campbell, G. Connard, D. Forel, S. A. Hall, C. J. Hoelting, and P. S. Millegan. We especially thank comments and suggested revisions from E. K. Biegert, R. J. Blakely, C., and L. Namazie. Two anonymous reviewers provided detailed comments which are greatly appreciated.

Disclaimer

The use of trade, firm or product names is purely for descriptive purposes and does not constitute an endorsement by the US Government.

Appendix A. Supplementary data

Supplementary data to this article can be found online at https://doi.org/10.1016/j.tecto.2026.231175.

References

Afonso, J.C., Salajegheh, F., Szwillus, W., Ebbing, J., Gaina, C., 2019. A global reference model of the lithosphere and upper mantle from joint inversion and analysis of multiple data sets. Geophys. J. Int. 217, 1602–1628. https://doi.org/10.1093/gji/ggz094.

Allen, P.A., Armitage, J.J., 2012. Cratonic basins. In: Busby, C., Azor, A. (Eds.), Tectonics of Sedimentary Basins: Recent Advances. Blackwell Publishing Ltd., pp. 602–620. https://doi.org/10.1002/9781444347166.ch30

Allen, P.A., Homewood, P., Williams, G.D., 1986. Foreland basins: an introduction. In: Allen, P.A., Homewood, P. (Eds.), Foreland Basins, 8. Blackwell Scientific Publications, International Association of Sedimentologists, pp. 3–12. https://doi.org/10.1002/9781444303810.

Allen, P.A., Eriksson, P.G., Alkmim, F.F., Betts, P.G., Catuneanu, O., et al., 2015. Classification of basins, with special reference to Proterozoic examples. In: Mazumder, R., Eriksson, P.G. (Eds.), Precambrian Basins of India: Stratigraphic and Tectonic Context, 43. Geological Society, Memoirs, pp. 5–28. https://doi.org/10.1144/M43.2.

Alvey, A., Gaina, C., Kusznir, N.J., Torsvik, T.H., 2008. Integrated crustal thickness mapping and plate reconstructions for the high Arctic. Earth Planet. Sci. Lett. 274, 310–321. https://doi.org/10.1016/j.epsl.2008.07.036.

Amante, C., Eakins, B.W., 2009. ETOPO1 1 arc-minute global relief model: procedures, data sources, and analysis. NOAA Technical Memorandum, NESDIS NGDC-24. https://doi.org/10.7289/V5C8276M.

Anderson, O.B., Kundsen, P., Berry, P.A.M., 2010. The DNSC08GRA global marine gravity field from double retracked satellite altimetry. J. Geod. 84, 191–199. https://doi.org/10.1007/s00190-009-0355-9.

Armitage, J.J., Allen, P.A., 2010. Cratonic basins and the long-term subsidence history of continental interiors. J. Geol. Soc. Lond. 167, 61–70. https://doi.org/10.1144/0016-76492009-108.

Bally, A. W., & Snelson, S. (1980). Realms of subsidence. A. D. Miall, Facts and Principles of World Petroleum Occurrence (pp. 9–94). Canadian Society of Petroleum Geologists, Memoir, 6.

Bally, A.W., Roberts, D.G., Sawyer, D., Sinkewich, A., 2020. Tectonic and basin maps of the world. In: Roberts, D.G., Bally, A.W. (Eds.), Regional Geology and Tectonics: Principles of Geologic Analysis, Chapter 27. Elsevier, pp. 761–862. https://doi.org/10.1016/B978-0-444-64134-2.00026-2.

Barbosa, V.C.F., Silva, J.B.C., 1994. Generalized compact gravity inversion. Geophysics 59, 57–68. https://doi.org/10.1190/1.1443534.

Bassin, C., Laske, G., Masters, G., 2000. The current limits of resolution for surface wave tomography in North America (F897). EOS, Trans. Am. Geophys. Union 81 (48).

Bauer, K., Neben, S., Shreckenberger, B., Emmermann, R., Hinz, K., Fechner, N., et al., 2000. Deep structure of the Namibia continental margin as derived from integrated geophysical studies. J. Geophys. Res. 105 (B11), 25829–25853. https://doi.org/10.1029/2000JB900227.

Bird, D.E., Hall, S.A., 2016. Early seafloor spreading in the South Atlantic: new evidence for M-series magnetochrons north of the Rio Grande Fracture Zone. Geophys. J. Int. 206, 835–844. https://doi.org/10.1093/gji/ggw147.

Bird, D.E., Burke, K., Hall, S.A., Casey, J.F., 2005. Gulf of Mexico tectonic history: hotspot tracks, crustal boundaries, and early salt distribution. Am. Assoc. Petrol. Geologists Bullet. 89 (3), 311–328. https://doi.org/10.1306/10280404026.

Blakely, R.J., 1995. Potential Theory in Gravity & Magnetic Applications. Cambridge University Press. https://doi.org/10.1017/CBO9780511549816.

Bradley, D.C., 2011. Secular trends in the geologic record and the supercontinent cycle. Earth Sci. Rev. 108, 16–33. https://doi.org/10.1016/j.earscirev.2011.05.003.

Buck, W.R., 2017. The role of magmatic loads and rift jumps in generating seaward dipping reflectors on volcanic rifted margins. Earth Planet. Sci. Lett. 466, 62–69. https://doi.org/10.1016/j.epsl.2017.02.041.

Burke, K., 2011. Plate tectonics, the Wilson Cycle, and mantle plumes: geodynamics from the top. Ann. Rev. Earth Planet. Sci. 39, 1–29. https://doi.org/10.1146/annurev-earth-040809-152521.

Busby, C., Azor, P.A., 2012. Tectonics of Sedimentary Basins: Recent Advances. Blackwell Publishing Ltd. https://doi.org/10.1002/9781444347166.

Calderon, Y., 2018. Structural architecture, sedimentary balance and hydrocarbon potential of a “wedgetop-foredeep” transition zone of retro-foreland basin: example of the Maranon and Huallaga basins of northern Peru (Publication ID tel-02078737) [Doctoral dissertation, Universite Paul Sabatier]. Hal Open Sci. 231. NNT: 2018TOU30038.

Carmichael, R.S., 1989. Practical Handbook of Physical Properties of Rocks and Minerals. CRC Press, Inc.

Chakravarthi, V., Sundararajan, N., 2007. 3D gravity inversion of basement relief – a depth-dependent density approach. Geophysics 72/,2, 123–132. https://doi.org/10.1190/1.2431634.

Chakravarthi, V., Sastry, S.R., Ramamma, B., 2013. MODTOHAFSD – a GUI based JAVA code for gravity analysis of strike limited sedimentary basins by means of growing bodies with exponential density contrast – depth variation: a space domain approach. Comput. Geosci. 56, 131–141. https://doi.org/10.1016/j.cageo.2013.02.005.

Charrier, R., Ramos, V.A., Tapia, F., Sagripanti, L., 2015. Tectono-stratigraphic evolution of the Andean Orogen between 31 and 37°S (Chile and western Argentina). In: Sepulveda, S.A., Giambiagi, L.B., Moreiras, S.M., Pinto, L., Tunik, M., Hoke, G.D., et al. (Eds.), Geodynamic processes in the Andes of central Chile and Argentina, 399. Geological Society, London, Special Publications, pp. 13–61. https://doi.org/10.1144/SP399.20.

Cheesman, S., MacLeod, I., Hollyer, G., 1998. A new, rapid, automated grid stitching algorithm. Explor. Geophys. 29 (4), 301–305. https://doi.org/10.1071/EG998301.

Chen, A., Jin, C., Lou, Z., Chen, H., Xu, S., Huang, K., et al., 2013. Salt tectonics and basin evolution in the Gabon coastal basin, West Africa. J. Earth Sci. 24/6, 903–917. https://doi.org/10.1007/s12583-013-0383-5.

Chorowicz, J., 2005. The East African rift system. J. Afr. Earth Sci. 43, 379–410. https://doi.org/10.1016/j.jafrearsci.2005.07.019.

Christensen, N.I., Mooney, W.D., 1995. Seismic velocity structure and composition of the continental crust: a global view. J. Geophys. Res. 100 (B7), 9761–9788. https://doi.org/10.1029/95JB00259.

Cloetingh, S.A.P.L., Negendank, J.F.W., 2010. Perspectives on integrated solid earth science. In: Cloetingh, S.A.P.L., Negendank, J.F.W. (Eds.), New Frontiers in Integrated Solid Earth Sciences. Springer Science + Business Media, pp. 1–37. https://doi.org/10.1007/978-90-481-2737-5_1.

Colli, L., Ghelichkhan, S., Bunge, H.-P., 2016. On the ration of dynamic topography and gravity anomalies in a dynamic Earth. Geophys. Res. Lett. 43. https://doi.org/10.1002/2016GL067929.

Cordell, L., 1973. Gravity analysis using an exponential density-depth function – San Jacinto Graben, California. Geophysics 38 (4), 684–690. https://doi.org/10.1190/1.1440367.

Decelles, P.G., 2012. Foreland basin systems revisited: Variations in response to tectonic settings. In: Busby, C., Azor, A. (Eds.), Tectonics of Sedimentary Basins: Recent Advances. Blackwell Publishing Ltd., pp. 405–426. https://doi.org/10.1002/9781444347166.ch20

DeCelles, P.G., Giles, K.A., 1996. Foreland basin systems. Basin Res. 8, 105–123. https://doi.org/10.1046/j.1365-2117.1996.01491.x.

Dick, H.J.B., Lissenberg, J., Warren, J.M., 2010. Mantle melting, melt transport, and delivery beneath a slow-spreading ridge: the paleo-MAR from 23°15’N to 23°45’N. J. Petrol. 51, 425–467. https://doi.org/10.1093/petrology/egp088.

Dickinson, W.R., 1974. Plate tectonics and sedimentation. In: Dickinson, W.R. (Ed.), Tectonics and Sedimentation, 22. Society of Economic Paleontologists and Mineralogists, Special Publication, pp. 1–27. https://doi.org/10.2110/pec.74.22.0001.

Dobrin, M.B., Savit, C.H., 1988. Introduction to Geophysical Prospecting. McGraw-Hill Book Company.

Dowla, N., 2019. Full-fit reconstruction of the Central Atlantic Ocean: 3D crustal models of eastern North America and Northwest Africa: Doctoral dissertation. University of Houston.. https://uh-ir.tdl.org/items/3dcabc3d-2a05-4b2b-bbdc-56f3dd14f448

Drinkwater, M.R., Floberghagen, R., Haagmans, R., Muzi, D., Popescu, A., 2003. GOCE: ESA’S first Earth explorer core mission. In: Beutler, G., Rummel, R., Drinkwater, M. R., von Steiger, R. (Eds.), Earth Gravity Field from Space – From Sensors to Earth Science. Dordrecht, Kluwer Academic Publishers, pp. 419–432.

Ebinger, C., Ayele, A., Kier, D., Rowland, J., Yirgu, G., Wright, T., et al., 2010. Length and timescales of rift faulting and magma intrusion: the Afar rifting cycle from 2005 to present. Annu. Rev. Earth Planet. Sci. 38, 439–466. https://doi.org/10.1146/annurev-earth-040809-152333.

Evans, D.A.D., Li, Z.X., Murphy, J.B., 2016. Four-dimensional context of earth’s supercontinents. In: Li, Z.X., Evans, D.A.D., Murphy, J.B. (Eds.), Supercontinent Cycles through Earth History. Geological Society, London, pp. 1–14. https://doi.org/10.1144/SP424.12. Special Publications 424.

Evenick, J.C., 2021. Glimpses into earth’s history using a revised global sedimentary basin map. Earth-Sci. Rev. 215, 103565. https://doi.org/10.1016/j.earscirev.2021.103564.

Flament, N., Gurnis, M., Mueller, R.D., 2013. A review of observations and models of dynamic topography. Lithosphere 5, 189–210. https://doi.org/10.1130/L245.1.

Foote, M., Miller, A., 2006. Principles of Paleontology, third edition. W. H. Freeman Company.

Forsberg, R., 1984. A study of terrain reductions, density anomalies and geophysical inversion methods in gravity field mapping. In: Reports of the Department of Geodetic Science and Surveying (355). Ohio State University. https://kb.osu.edu/handle/1811/105127.

Forsberg, R., Skourup, H., 2005. Arctic Ocean gravity, geoid and sea-ice freeboard heights from ICESat and GRACE. Geophys. Res. Lett. 32, L21502. https://doi.org/10.1029/2005GL023711.

Fowler, C.M.R., 2005. The Solid Earth: An Introduction to Global Geophysics. Cambridge University Press.

France-Lanord, C., Derry, L., Michard, A., 1993. Evolution of the Himalaya since Miocene time: Isotopic and sedimentological evidence from the Bengal Fan. In: Treloar, P.J., Searle, M.P. (Eds.), Himalayan Tectonics. Geological Society, London, pp. 603–621. https://doi.org/10.1144/GSL.SP.1993.074.01.4. Special Publications, 74.

Frisch, W., Meschede, M., Blakey, R., 2011. Plate Tectonics, Continental Drift and Mountain Building. Springer. https://doi.org/10.1007/978-3-540-76504-2_11.

Fritz, R.D., Mitchell, J.R., 2021. The Anadarko “Super” basin: 10 key characteristics to understand its productivity. Am. Assoc. Petrol. Geol. Bullet. 105 (6), 1199–1231. https://doi.org/10.1306/03242120082.

Fullea, J., Lebedev, S., Martinec, Z., Celli, N.L., 2021. WINTERC-G: mapping the upper thermochemical heterogeneity from coupled geophysical – petrological inversion of seismic waveforms, heat flow, surface elevation and gravity satellite data. Geophys. J. Int. 226, 149–191. https://doi.org/10.1093/gji/ggab094.

Galloway, W.E., 2008. Depositional evolution of the Gulf of Mexico sedimentary basin. In: Miall, A.D. (Ed.), The Sedimentary Basins in the United States and Canada (Pp 505–549), K. J. Hsu (Ser. Ed.), Sedimentary Basins of the World 5. Elsevier. https://doi.org/10.1016/S1874-5997(08)00015-4.

Global Heat Flow Data Assessment Group, Fuchs, S., Neumann, F., Norden, B., Balkan-Pazvantoglu, E., Elbarbary, S., et al., 2024. The Global Heat Flow Database: Release 2024, 1. GFZ Data Services. https://doi.org/10.5194/egusphere-egu24-16952.

Grauch, V.J.S., Connell, S.D., 2013. New perspectives on the geometry of the Albuquerque Basin, Rio Grande rift, New Mexico: Insights from geophysical models

of rift-fill thickness. In: Hudson, M.R., Grauch, V.J.S. (Eds.), New Perspectives on Rio Grande Rift Basins: From Tectonics to Groundwater. Geological Society of America, pp. 427–462. https://doi.org/10.1130/2013.2494(16). Special Paper, 494.
Grenholm, M., Schersten, A., 2015. A hypothesis for Proterozoic-Phanerozoic supercontinent cyclicity, with implications for mantle convection, plate tectonics and Earth system evolution. Tectonophysics 662, 434–453. https://doi.org/10.1016/j.tecto.2015.04.009.
Grevemeyer, I., Weigel, W., Jennrich, C., 1998. Structure and aging of oceanic crust at 14°S on the East Pacific rise. Geophys. J. Int. 135, 573–584. https://doi.org/10.1046/j.1365-246X.1998.00673.x.
Grozinger, J., Jordan, T.H., 2020. Understanding Earth, eighth edition. W. H. Freeman and Company.
Harris, P.M., Moore, C.H., Wilson, J.L., 1985. Carbonate platforms. In: Warme, J.E., Shanley, K.W. (Eds.), Carbonate Depositional Environments, Modern and Ancient, part 2: carbonate platforms. Colorado School of Mines, Quarterly, 80/4, pp. 31–60.
Hartley, R.W., Allen, P.A., 1994. Interior cratonic basins of Africa: relation to continental break-up and role of mantle convection. Basin Res. 6 (2–3), 95–113. https://doi.org/10.1111/j.1365-2117.1994.tb00078.x.
Heirtzler, J.R., 1969. The theory of sea floor spreading. Naturwissenschaften 56, 341–347. https://doi.org/10.1007/BF00596921.
Heirtzler, J.R., Dickson, G.O., Herron, E.M., Pitman III, W.C., Le Pichon, X., 1968. Marine magnetic anomalies, geomagnetic field reversals, and motions of the ocean floor and continents. J. Geophys. Res. 73 (6), 2119–2136. https://doi.org/10.1029/JB073i006p02119.
Hinze, W.J., von Frese, R.R.B., Saad, A.H., 2013. Gravity and Magnetic Exploration: Principles, Practices, and Applications. Cambridge University Press.
Hooft, E.E.E., Detrick, R.S., Toomey, D.R., Collins, J.A., Lin, J., 2000. Crustal thickness and structure along three contrasting spreading segments of the Mid-Atlantic Ridge, 33.5°-35°N. J. Geophys. Res. 105 (B4), 8205–8226. https://doi.org/10.1029/1999JB900442.
Hyman, A., 2017. Principles of Paleoclimatology. Calisto References.
Ingersoll, R.V., 2012. Tectonics of sedimentary basins, with revised nomenclature. In: Busby, C., Azor, P.A. (Eds.), Tectonics of Sedimentary Basins: Recent Advances. Blackwell Publishing Ltd., pp. 3–43. https://doi.org/10.1002/9781444347166.ch1
Jacome, M.I., Kusznir, N., Audemard, F., Flint, S., 2003. Formation of the Maturin foreland basin, eastern Venezuela: thrust sheet loading or subduction dynamic topography. Tectonics 22 (5), 1046. https://doi.org/10.1029/2002TC001381.
Kaban, M.K., Schwintzer, P., Tikhotsky, S.A., 1999. A global isostatic gravity model of the Earth. Geophys. J. Int. 136, 519–536. https://doi.org/10.1046/j.1365-246x.1999.00731.x.
Kenyon, S., Forsberg, R., Coakley, B., 2008. New gravity field for the Arctic: *EOS*. Trans. Am. Geophys. Union 89 (32), 289–290. https://doi.org/10.1029/2008EO320002.
Kingston, D.R., Dishroon, C.P., Williams, P., A., 1983. Global basin classification system. Am. Assoc. Pet. Geol. Bull. 67 (12), 2175–2193. https://doi.org/10.1306/AD460936-16F7-11D7-8645000102C1865D.
Klein, G., deV., 1995. Intracratonic basins. In: Busby, C.J., Ingersoll, R.V., R. V. (Eds.), Tectonics of Sedimentary Basins. Blackwell Science, Inc., pp. 459–478
Kusznir, N.J., Karner, G.D., 2007. Continental lithospheric thinning and breakup in response to upwelling divergent mantle flow: applications to the Woodlark, Newfoundland and Iberia margins. In: Karner, G.D., Manatschal, G., Pinheiro, L.M. (Eds.), Imaging, Mapping and Modelling Continental Lithosphere Extension and Breakup, 282. Geological Society, London, Special Publications, pp. 389–419. https://doi.org/10.1144/SP282.16.
Laske, G., Masters, G., Ma, Z., Pasyanos, M., 2012. CRUST1.0: an updated global model of Earth's CRUST: *European Geophysical Union*. Geophysical Res. Abstract 14. EGU2012-3743-1. http://igppweb.ucsd.edu/gabi/crust1.html.
Laursen, J., Scholl, D.W., von Huene, R., 2002. Neotectonic deformation of the Central Chile margin: deepwater forearc basin formation in response to hot spot ridge and seamount subduction. Tectonics 21 (5), 1038. https://doi.org/10.1029/2001TC901023.
Lemoine, F.G., Kenyon, S.C., Factor, J.K., Trimmer, R.G., Pavlis, N.K., Chinn, D.S., et al., 1998. The Development of the Joint NASA GSFC and the National Imagery and Mapping Agency (NIMA) Geopotential Model EGM96. National Aeronautics and Space Administration, Goddard Space Flight Center, NASA/TP-1998-206861.
Li, Y., Oldenburg, D.W., 1998. 3-D inversion of gravity data. Geophysics 63, 109–119. https://doi.org/10.1190/1.1444302.
Liang, W., Jiancheng, L., Xinyu, X., Zhang, S., Zhao, Y., 2020. A high-resolution Earth's gravity field model SGG-UGM-2 from GOCE, GRACE, satellite altimetry, and EGM2008. Engineering 6, 860–878. https://doi.org/10.1016/j.eng.2020.05.008.
Lin, P., 2018. Crustal Structure and Tectonostratigraphic Evolution of the Eastern Gulf of Mexico Basin. Doctoral dissertation. University of Houston. https://uh-ir.tdl.org/items/3bae78e6-69ff-4e05-81b0-104c92d630ba.
Lin, P., Bird, D.E., Mann, P., 2019. Crustal structure of an extinct, late Jurassic-to-earliest cretaceous spreading center and its adjacent oceanic crust in the eastern Gulf of Mexico. Marine Geophys. Res. 40, 395–418. https://doi.org/10.1007/s11001-019-09379-5.
Liu, M., 2021. Mesozoic Rift Evolution and Crustal Structure of the Gulf of Mexico Basin from Integration of Multiple Geological and Geophysical Datasets. Doctoral dissertation. University of Houston. https://uh-ir.tdl.org/items/020b6f39-5b0d-43a6-86fa-01c09c346378.
Loureiro, P., 2017. Early Cretaceous Tectonostratigraphic Evolution of Rift and Sag Basins of the Campos and Santos Basins, Southeastern Brazil, Using Potential Fields, Seismic Reflection, and Well Data. Doctoral dissertation. University of Houston. https://uh-ir.tdl.org/items/a04b7f17-1526-4a49-b180-3d2858768d5c.
Lunn, E.M., 2019. 3-D crustal modeling of the Barreirinhas and Ceara Basins of northeastern Brazil: Master's thesis. University of Houston https://uh-ir.tdl.org/items/449afc34-d63c-4112-a765-6687bb502dea.
Marshak, S., 2022. Earth: Portrait of a Planet, Seventh edition. W.W Norton & Company.
Masy, J., Niu, F., Levander, A., Schmitz, M., 2015. Lithospheric expression of Cenozoic subduction, Mesozoic rifting and the Precambrian Shield in Venezuela. Earth Planet. Sci. Lett. 410, 12–24. https://doi.org/10.1016/j.epsl.2014.08.041.
Mayer-Gürr, T., 2007. ITG-Grace03s: The Latest GRACE Gravity Field Solution Computed in Bonn. Joint International GSTM and SPP Symposium, Potsdam, Germany.
McKenzie, D.P., 1967. Some remarks on heat flow and gravity anomalies. J. Geophys. Res. 12 (24), 6261–6273. https://doi.org/10.1029/JZ072i024p06261.
Miall, A.D., 2010. The Geology of Stratigraphic Sequences, Second edition. Springer.
Miall, S.D., 2000. Principles of Sedimentary Basin Analysis, Third edition. Springer.
Molinari, I., Morelli, A., 2011. EPcrust: a reference crustal model for the European Plate. Geophys. J. Int. 185, 352–364. https://doi.org/10.1111/j.1365-246X.2011.04940.x.
Mooney, W.D., 2015. Crust and lithospheric structure: The global Earth's crust. In: Romanowicz, B., Dziewonski, A. (Eds.), Seismology and Structure of the Earth: Treatise on Geophysics, 1. Elsevier, pp. 81–165. https://doi.org/10.1016/B978-044452748-6.00011-0.
Mooney, W.D., Kaban, M.K., 2010. The north American upper mantle: density, composition, and evolution. J. Geophys. Res. 115, B12424. https://doi.org/10.1029/2010JB000866.
Mooney, W.D., Laske, G., Masters, T.G., 1998. CRUST 5.1: a global crustal model at 5°× 5°. J. Geophys. Res. 103 (B1), 727–747. https://doi.org/10.1029/97JB02122.
Mooney, W.D., Barrera-Lopez, C., Suarez, M.G., Castelblanco, M.A., 2023. Earth Crustal Model 1 (ECM1): A 1° x 1° global seismic and density model. Earth-Sci. Rev. 243, 104493. https://doi.org/10.1016/j.earscirev.2023.104493.
Moores, E.M., Twiss, R.J., 1995. Tectonics. W. H. Freeman and Company.
Müller, R.D., Sdrolias, M., Gaina, C., Roest, W.R., 2008. Age, spreading rates, and spreading asymmetry of the world's ocean crust. Geochem. Geophys. Geosyst. 9 (4), Q04006. https://doi.org/10.1029/2007GC001743.
Müller, R.D., Seton, M., Zahirovic, S., Williams, S.E., Matthews, K.J., Wright, N.M., et al., 2016. Ocean basin evolution and global-scale plate reorganization events since Pangea breakup. Annu. Rev. Earth Planet. Sci. 44, 107–138. https://doi.org/10.1146/annurev-earth-060115-012211.
Murphy, J.B., Nance, R.D., 2013. Speculations on the mechanisms for the formation and breakup of supercontinents. Geosci. Front. 4, 185–194. https://doi.org/10.1016/j.gsf.2012.07.005.
Nance, R.D., Murphy, J.B., Santosh, M., 2014. The supercontinent cycle: a retrospective essay. Gondw. Res. 25, 4–29. https://doi.org/10.1016/j.gr.2012.12.026.
Nguyen, L.C., 2015. Rigid and Non-rigid Plate Reconstruction of the East Africa and Antarctica Continental Margins. Master's Thesis. University of Houston. https://uh-ir.tdl.org/items/d0f64141-4e6d-490b-beb0-9d7cc34d8785.
Nguyen, L.C., Hall, S.A., Bird, D.E., Ball, P.J., 2016. Reconstruction of the East Africa and Antarctica continental margins. J. Geophys. Res. Solid Earth 121, 4156–4179. https://doi.org/10.1002/2015JB012776.
Noda, A., 2016. Forearc basins: types, geometries, and relationships to subduction zone dynamics. Geol. Soc. Am. Bull. 128, 879–895. https://doi.org/10.1130/B31345.1.
O'Grady, D.B., Syvitski, J.P.M., Pratson, L., Sarg, J.F., 2000. Categorizing the morphologic variability of siliciclastic passive continental margins. Geology 28 (3), 207–210. https://doi.org/10.1130/0091-7613(2000)28<207:CTMVOS>2.0.CO;2.
Oldenburg, D.W., 1974. The inversion and interpretation of gravity anomalies. Geophysics 39, 526–536. https://doi.org/10.1190/1.1440444.
Osmundsen, P.T., Redfield, T.F., 2011. Crustal taper and topography at passive continental margins. Terra Nova 23 (6), 349–361. https://doi.org/10.1111/j.1365-3121.2011.01014.x.
Parker, R.L., 1973. The rapid calculation of potential anomalies. Geophys. J. Roy. Astron. Soc. 31, 447–455. https://doi.org/10.1111/j.1365-246X.1973.tb06513.x.
Parker, R.L., Huestis, S.P., 1974. The inversion of magnetic anomalies in the presence of topography. J. Geophys. Res. 79 (11), 1587–1593. https://doi.org/10.1029/JB079i011p01587.
Pasyamos, M.E., Masters, T.G., Laske, G., Ma, Z., 2014. LITHO 1.0: an updated crust and lithospheric model of the Earth. J. Geophys. Res. Solid Earth 119, 2153–2173. https://doi.org/10.1002/2013JB010626.
Pavlis, N.K., Holmes, S.A., Kenyon, S.C., Factor, J.K., 2012. The development and evaluation of the Earth Gravitational Model 2008 (EGM2008). J. Geophys. Res. 117 (B4), B04406. https://doi.org/10.1029/2011JB008916.
Pedersen, L.B., 1979. Constrained inversion of potential field data. Geophys. Prospect. 27, 726–748. https://doi.org/10.1111/j.1365-2478.1979.tb00993.x.
Perry, H.K.C., Jaupart, C., Mareschal, J.-C., Shapiro, N.M., 2006. Upper mantle velocity-temperature conversion and composition determined from seismic refraction and heat flow. J. Geophys. Res. 111, B07301. https://doi.org/10.1029/2005JB003921.
Peters, G., van Balen, R.T., 2007. Tectonic geomorphology of the northern Upper Rhine Graben, Germany. Global Planet. Change 58, 310–334. https://doi.org/10.1016/j.gloplacha.2006.11.041.
Peterson, J.A., MacCary, L.M., 1987. Regional stratigraphy and general petroleum geology of the U.S. portion of the Williston Basin and adjacent areas. In: Peterson, J. A., Kent, D.M., Anderson, S.B., Pilatzke, R.H., Longman, M.W. (Eds.), Williston Basin: Anatomy of a Cratonic Oil Province. Rocky Mountain Association of Geologists, pp. 9–44.
Pratsch, J.-C., 1986. The distribution of major oil and gas reserves in regional basin structures – an example from the Powder River Basin, Wyoming, USA. J. Petrol. Geol. 9, 393–412. https://doi.org/10.1111/j.1747-5457.1986.tb00401.x.
Prodehl, C., Mooney, W.D., 2012. Exploring the Earth's Crust: History and Results of Controlled-Source Seismology. Geological Society of America, Memoir, p. 208.

Rapp, R.H., 1997. The use of potential coefficient models for geoid undulation determinations using a spherical harmonic representation of the height anomaly/geoid undulation difference. J. Geodesy 71, 282–289. https://doi.org/10.1007/s001900050096.

Reguzzoni, M., Sampietro, D., 2015. GEMMA: an earth crustal model based on GOCE satellite data. Int. J. Appl. Earth Observat. Geoinform. 35, 31–43. https://doi.org/10.1016/j.jag.2014.04.002.

Reid, I., Jackson, H.R., 1981. Oceanic spreading rate and crustal thickness. Mar. Geophys. Res. 5, 165–172. https://doi.org/10.1007/BF00163477.

Romito, S., 2021. Crustal Structure, Tectonostratigraphy, and Hydrocarbon Potential of the Terranes Underlying the Caribbean Plate and the Camamu-Almada Rifted Passive Margin of Northeastern Brazil. Doctoral dissertation. University of Houston. https://uh-ir.tdl.org/items/e641127a-6f65-4012-8897-c7bb49f8caef.

Rosendahl, B.R., Reynolds, D.J., Lorber, P.M., Burgess, C.F., McGill, J., Scott, D., et al., 1986. Structural expressions of rifting: lessons from Lake Tanganyika, Africa. In: Frostick, L.E., Renaut, R.W., Reid, I., Tiercelin, J.J. (Eds.), Sedimentation in the African Rifts. Geological Society, London, Special Publications, 25, pp. 29–43. https://doi.org/10.1144/GSL.SP.1986.025.01.04.

Roure, P., 2014. Crustal architecture, thermal evolution and energy resources of compressional basins. Geol. Belg. 17 (2), 182–194. https://popups.uliege.be/1374-8505/index.php?id=4577.

Rüpke, L.H., Schmalholz, S.M., Schimid, D.W., Podlad-chikov, Y.Y., 2008. Automated thermo-tectonostratigraphic basin reconstruction: Viking Graben case study. Am. Assoc. Petrol. Geologists Bullet. 92, 309–326. https://doi.org/10.1306/11140707009.

Sandwell, D.T., Smith, W.H.F., 2009. Global marine gravity from retracked Geosat and ERS-1 altimetry: ridge segmentation versus spreading rate. J. Geophys. Res. 114 (B01), B01411. https://doi.org/10.1029/2008JB006008.

Sandwell, D.T., Müller, R.D., Smith, W.H.F., Garcia, E., Francis, R., 2014. New global marine gravity model from CryoSat-2 and Jason-1 reveals buried tectonic structure. Science 346 (6205), 65–67. https://doi.org/10.1126/science.1258213.

Scheck-Wenderoth, M., Maystrenko, Y., Hubscher, C., Hansen, M., Mazur, S., 2008. Dynamics of salt basins. In: Littke, R., Bayer, U., Gajewski, D., Nelskamp, S. (Eds.), Dynamics of Complex Intracontinental Basins: The Central European Basin System. Springer, pp. 307–322. https://gfzpublic.gfz-potsdam.de/pubman/item/item_237971.

Scheinert, M., Ferraccioli, F., Schwabe, J., Bell, R., Studinger, M., Damaske, D., et al., 2016. New Antarctic gravity anomaly grid for enhanced geodetic and geophysical studies in Antarctica. Geophys. Res. Lett. 43, 600–610. https://doi.org/10.1002/2015GL067439.

Schmitz, M., Avila, J., Bezada, M., Viera, E., Yanez, M., Levander, A., et al., 2008. Crustal thickness variations in Venezuela from deep seismic observations. Tectonophysics 459 (1–4), 14–26. https://doi.org/10.1016/j.tecto.2007.11.072.

Sclater, J.G., Jaupart, C., Galson, D., 1980. The heat flow through oceanic and continental crust and the heat loss of the Earth. Rev. Geophys. Space Phys. 18 (1), 269–311. https://doi.org/10.1029/RG018i001p00269.

Sharma, P.V., 1976. Geophysical methods in geology. In: Methods in Geochemistry and Geophysics, Fourth edition. Elsevier, p. 12.

Stein, C.A., Stein, S., 1992. A model for the global variation in oceanic depth and heat flow with lithospheric age. Nature 359 (6391), 123–129. https://doi.org/10.1038/359123a0.

Straume, E.O., Gaina, C., Medvedev, S., Hochmuth, K., Gohl, K., Whittaker, J.M., et al., 2019. GlobSed: updated total sediment thickness in the world's oceans. Geochem. Geophys. Geosyst. 20, 1756–1772. https://doi.org/10.1029/2018GC008115.

Stüwe, K., 2007. Geodynamics of the Lithosphere, Second edition. Springer.

Sutra, E., Manatschal, G., 2012. How does the continental crust thin in a hyperextended rifted margin? Insights from the Iberia margin. Geology 40 (2), 139–142. https://doi.org/10.1130/G32786.1.

Tapley, B.D., Bettadpur, S., Watkins, M., Reigber, C., 2004. The gravity recovery and climate experiment: mission overview and early results. Geophys. Res. Lett. 31 (9), L09607. https://doi.org/10.1029/2004GL019779.

Telford, W.M., Geldart, L.P., Sheriff, R.E., Keys, D.A., 1976. Applied Geophysics. Cambridge University Press.

Tesauro, M., Kaban, M.K., Cloetingh, S.A.P.L., 2009. A new thermal and rheological model of the European lithosphere. Tectonophysics 476, 478–495. https://doi.org/10.1016/j.tecto.2009.07.022.

Tufano, B.C., Pietras, J.T., 2017. Coupled flexural-dynamic subsidence modeling approach for retro-foreland basins: example from the Western Canada Sedimentary Basin. Geol. Soc. Am. Bull. 129, 1622–1635. https://doi.org/10.1130/B31646.1.

Tugend, J., Fillard, M., Manatschal, G., Nirrengarten, M., Harkin, C., Epin, M.-E., et al., 2020. Reappraisal of the magma-rich versus magma-poor rifted margin archetypes. In: McClay, K.R., Hammerstein, J.A. (Eds.), Passive Margins: Tectonics, Sedimentation and Magmatism. Geological Society, London, Special Publications, 476, pp. 23–47. https://doi.org/10.1144/SP476.9.

Turcotte, D.L., Schubert, G., 2002. Geodynamics, Second edition. Cambridge University Press.

Watts, A.B., 1992. The effective elastic thickness of the lithosphere and the evolution of foreland basins. Basin Res. 4, 169–178. https://doi.org/10.1111/j.1365-2117.1992.tb00043.x.

Watts, A.B., 2001. Isostasy and Flexure of the Lithosphere. Cambridge University Press.

Watts, A.B., 2012. Models for the evolution of passive margins. In: Roberts, D.G., Bally, A.W. (Eds.), Regional Geology and Tectonics: Principles of Geologic Analysis, Chapter 11. Elsevier, 1A, pp. 311–328.

Weber, J.C., Dixon, T.H., DeMets, C., Ambeth, W.B., Jansma, P., Mattioli, G., et al., 2001. GPS estimate of relative motion between the Caribbean and South American plates, and geologic implications for Trinidad and Venezuela. Geology 29 (1), 75–78. https://doi.org/10.1130/0091-7613(2001)029<0075:GEORMB>2.0.CO;2.

Weeks, L.G., 1952. Factors of sedimentary basin development that control oil occurrence. Bull. Am. Assoc. Pet. Geol. 36 (1), 2071–2124. https://doi.org/10.1306/5CEADBBD-16BB-11D7-8645000102C1865D.

White, R.S., McKenzie, D., O'Nions, R.K., 1992. Oceanic crustal thickness from seismic measurements and rare earth element inversions. J. Geophys. Res. 97 (B13), 19683–19715.

Withjack, M.O., Schlische, R.W., Olsen, P., 2002. Rift-basin Structure and its Influence on Sedimentary Systems, 73. Society for Sedimentary Geology (SEPM), Special Publication, pp. 57–81. https://doi.org/10.2110/pec.02.73.0057.

Zhang, H., 2021. Gravity Modeling, Seismic Stratigraphy, and Thermal Maturity Modeling of Hydrocarbons of the Permian Foreland Basin, USA and the Sergipe-Alagoas Rifted-Passive Margin, Brazil. Doctoral dissertation. University of Houston. https://uh-ir.tdl.org/items/165fed43-b4eb-4bb8-a2e6-f50aac532d39.

Zhang, H., Mann, P., Bird, D.E., Rudolph, K., 2021. Integration of regional gravity modeling, subsidence analysis, and source rock maturity data to understand the tectonic and hydrocarbon evolution of the Permian Basin, West Texas. Interpretation 9 (1), T161–T181. https://doi.org/10.1190/INT-2020-0065.1.

Zhou, D., Li, C.-F., Zlotnik, S., Wang, J., 2020. Correlations between oceanic crustal thickness, melt volume, and spreading from global gravity observation. Marine Geophys. Res. 41 (3), 14. https://doi.org/10.1007/s11001-020-09413-x.